THESIS

THE IMPACTS OF THERMOKARST ACTIVITY ON A STREAM IN THE MCMURDO DRY VALLEYS

Submitted by

Zachary William Sudman

Department of Civil and Environmental Engineering

In partial fulfillment of the requirements

For the Degree of Master of Science

Colorado State University

Fort Collins, Colorado

Summer 2015

Master's Committee:

Advisor: Michael Gooseff

Brian Bledsoe
Ellen Wohl

ABSTRACT

THE IMPACTS OF THERMOKARST ACTIVITY ON A STREAM IN THE MCMURDO DRY VALLEYS

The McMurdo Dry Valleys (MDV) of Antarctica are a unique ice-free landscape that is host to vibrant ecosystems despite the harsh environment (<10 cm water equivalent/yr, -20°C mean air temperature). Aquatic ecosystems in the MDV are dependent on the ephemeral glacial runoff streams which feed the closed basin perennially ice covered lakes. The upland zones of the Dry Valleys have been shown to have some of the slowest ground surface change rates in the world. However, recent observations in the coastal valley transition zones suggest that this area may be nearing a threshold of rapid landscape change.

One of the recent observations that supports this idea is the discovery of extensive thermokarst degradation (permafrost thaw features) along the banks of Crescent Stream in Taylor Valley. In 2012, a large stretch of the West Branch of Crescent Stream was found to have significant thermokarst bank failures, while the adjacent East Branch was found to be unaffected. The thermokarst impacts within this setting are important to understand because of the disturbances that massive sediment loading can impose on downstream biological communities.

Annually repeated terrestrial LiDAR scans (3) were compared to determine the rates of ground surface change due to thermokarst degradation. It was found that the areal extent of the thermokarst was decreasing, however the average linear rates of retreat remained constant. Field

measurements including, pebble counts, fine sediment counts, and sieve samples were analyzed to determine the effects of the thermokarst on the stream bed material. It was found that the West Branch and the reach downstream of the confluence were consistently finer than the unaffected East Branch. This suggests that the finer bed material is due to the thermokarst bank degradation. Stream power was calculated for multiple reaches to be used as a metric for the mobilization of the streambed material. It was found that both branches infrequently experience flows substantial enough to mobilize the bed material. Even the finer bed material of the impacted West Branch reach required flows that had a 5 % chance of exceedance for mobilization of the bed. These findings suggest the West Branch of Crescent Stream and the biota supported by this branch of the stream, continue to adjust to the sediment introduced from the thermokarst bank degradation.

ACKNOWLEDGEMENTS

I would like to thank everyone who has helped me with this project along the way. I want to thank my fellow graduate students for the countless hours of sharing ideas, and offering insight. I want to thank my committee for helping to guide this project as it developed. I also want to thank my advisor Mike Gooseff. You helped guide and encourage me throughout this process, while still allowing me to learn on my own. You also gave me the opportunity of a lifetime to travel to Antarctica. This trip opened my eyes to the exciting possibilities of science, and the amazing technologies which allow us to live comfortably in such remote conditions. I learned so much about myself on this trip, and I will never forget this truly amazing experience.

I would also like to thank my friends and family for the continued support throughout this process. Most importantly I would like to thank my mother and father. Thank you guys for everything. You guys have always been there encouraging me never to settle and to follow my dreams. I have had an amazing experience taking your advice thus far, and we will see what exciting adventures lay ahead for me.

TABLE OF CONTENTS

LIST OF TABLES

LIST OF FIGURES

1. INTRODUCTION

The McMurdo Dry Valleys (MDVs) are a unique set of unglaciated valleys in Antarctica, located between the Transantarctic Mountains to the west, and the McMurdo Sound to the east. The MDVs are considered one of the driest, coldest deserts on earth with a mean annual air temperature of -18^{o}C, receiving less than 10 cm of water equivalent of precipitation a year [*Gooseff et al.*, 2011]. Despite these unforgiving conditions, life exists in the Dry Valleys and its persistence is largely dependent on the hydrologic cycle, which is strongly dictated by climate. The hydrology in this location is unique because the surface energy balance has a much stronger influence on hydrology than does precipitation [*Gooseff et al.*, 2011]. The limited precipitation that does fall in the Dry Valleys does not directly contribute to streamflow because once it falls and accumulates, it is quickly lost to sublimation [*Conovitz et al.*, 1998]. The 24 hour solar radiation, and the warmer air temperatures during the austral summers provide enough energy to melt the ice on the surface of the glaciers to produce runoff. The glacial runoff collects to form streams, which flow down the valleys and typically terminate at closed basin, perennially ice-covered lakes.

These ephemeral streams begin to flow around mid-November, and they cease flowing around late January. However, this range is highly dependent on the specific stream, and the weather patterns during each season. The solar aspect of the glaciers is the primary control on stream flow because the glacial runoff is virtually the only source of water contributing to these streams. This unique hydrologic control causes significant fluctuations in stream flow throughout the day based on the position of the sun, and topographic relief [*Conovitz et al.*, 1998]. The hydrologic variability is not only limited to diurnal cycles, these streams have also

been found to have high inter-annual variation in stream flow, with some annual peak stream flows shown to vary by five times from year to year [*McKnight et al.*, 1999].

The streams of the Dry Valleys flow from the glaciers to the lakes over an unconsolidated alluvium that is affected by periglacial processes. The active layer of the soils (the surface layer that experiences temperatures greater than freezing every year) extends to about 0.5 m in depth [*McKnight et al.*, 1999]. The typical stream channel is relatively wide (wider than the extent of peak annual flows), and composed of a coarse surface layer of bed material underlain by finer sub-surface material, a phenomenon known as armoring. The stability of the streams is largely due to the armoring of the channel bed, and the inability of these streams to mobilize this layer. These characteristics describe a generic type of channel that may be found in many reaches of the various Dry Valley streams, however the unique morphologic features expressed in each stream appear to be controlled by topography, hydraulics, and periglacial processes [*Fountain et al.*, 1999].

With the highly variable flow rates, short flow season, and harsh environmental conditions it would not be surprising if these streams were completely barren of life, however this is not the case. The streams of the Dry Valleys actually support an ecosystem under these extreme conditions by providing the necessary transportation of water, energy, and matter across the landscape. [*Gooseff et al.*, 2011]. The importance of the streams is not limited to the communities within the streams themselves. The streams are also critically important to the biological communities living in the soil of the wetted channel margins, and to the communities in the receiving lakes.

Unlike temperate streams, the ecosystems that exist in these streams are very basic with no macroscopic consumers or insects. The primary community found in the Dry Valley streams

is cyanobacteria, although there are also chlorophytes and diatoms [*McKnight et al.*, 1999]. These algal communities each prefer different habitats, and conditions within the streams. Algal abundance has been found to be greatest in stable stream reaches with stone pavements, or channel bed armoring [*McKnight et al.*, 1999]. In shallow depositional reaches near the outlets of lakes, algal growth can be limited by the instability of the sandy substrate [*Alger et al.*, 1997]. Biological communities of the lakes also depend on the conditions of the incoming stream channels. For example, primary production in West Lake Bonney, located at the upper reaches of Taylor Valley, was reduced 23% due to an increase in water turbidity due to sediment transported from the stream [*Foreman et al.*, 2004]. These observations suggest the geomorphic stream properties have a strong influence on the ecology of the streams and receiving lakes, and therefore the geomorphic processes of the streams are important to understand in the context of the ecology of the Dry Valleys.

Although the geomorphology of the streams is important to understand because of its potential impacts on the stream and lake biological communities, there has been little research done to investigate geomorphic processes on these unique streams. The lack of research in this area is likely due to the notion that this landscape, and these streams are relatively stable. This is true for some of the areas in the Dry Valleys. The stable upland zones have some of the slowest surface change rates measured in the world [*Marchant and Head*, 2007]. However, recent observations in the lower coastal zones, where the streams exist, suggest that this landscape is changing at rates greater than ever observed in this area [*Levy et al.*, 2013; *Fountain et al.*, 2014]. Many of these observations have been in locations where the permafrost or buried ice has thawed causing failures in the soil structure.

Thermokarst is a term used to describe landforms and processes that are the result of thawing permafrost [*Kokelj and Jorgenson*, 2013]. Thermokarst features play a significant role in shaping the landscape throughout the world's permafrost regions, including Antarctica. There are many diverse forms of thermokarst which are dictated by the topography of the landscape and the processes driving the melting ground ice. Retrogressive thaw slumps are a form of thermokarst that are often associated with streams. The mechanisms that initiate the formation of these features are typically erosion due to fluvial processes, or thermal subsidence [*Kokelj et al.*, 2009]. Understanding the impacts of thermokarst activity is increasingly important in the MDV, because of the widespread prevalence of permafrost and the amplification of these driving mechanisms due to a warming climate.

Thermokarst features not only influence the topography of a landscape, but they can have significant impacts on downstream biological communities. Streams with retrogressive thaw slumps have been found to have suspended sediment and solute concentrations that were several orders of magnitude higher than adjacent, unaffected streams [*Kokelj et al.*, 2013]. One study found that a thermokarst feature was responsible for introducing more sediment to a river than would typically be delivered over 18 years [*Bowden et al.*, 2008]. These abrupt changes to sediment loads have significant impacts on the geomorphic properties of the streams, and consequently adverse effects on the biota of the stream.

Most of thermokarst research has been done in the Arctic because it is a major driver of landscape change in this region and it impacts the people living there. Only recently have scientists begun to look at these same processes in Antarctica. Levy et al. (2013), documented retreat rates of a significant thermokarst feature in Garwood Valley on the Garwood River that had wasting rates on the order of ten times the estimated Holocene rates. This finding suggests

that the rates of thermokarst erosion have been increasing in the MDV. Therefore it has become increasingly important to begin to understand the impacts of these features on the landscape, hydrology, and ecology.

Figure 1. Images of thermokarst impacts on the West Branch of Crescent Stream taken upon discovery in January of 2012. Note armoring or desert pavement of bank material in photo on the left (thin top coarse layer underlain by fine material).

Significant thermokarst activity was discovered on the West Branch of Crescent Stream (Fryxell Basin, Taylor Valley see Figure 2) in January of 2012. There were significant bank failures that introduced large amounts of sediment to the active stream channel, and left sharp exposed banks where the sediment had failed (Figure 1). However, the nearby and very similar East Branch of Crescent Stream was found to be entirely unaffected. The thermokarst activity was documented along a significant reach of the West Branch. Site visits each year since 2012 have documented continued degradation of the banks each year. However, the subsequent impacts have been nowhere near the initial severity discovered in 2012.

This study addresses two main research objectives. The first objective is to determine the rate at which the thermokarst activity is changing the ground surface on the banks of the West Branch of Crescent Stream. These rates were determined by comparing repeat, annual terrestrial LiDAR scans of the impacted area to detect changes in the ground surface elevation. The second objective is to determine the impacts of the thermokarst activity on the bed material composition of the West Branch of Crescent Stream. This objective was addressed by conducting sediment size analysis of a variety of in-stream and near-stream sediments. This included fine sediment counts, pebble counts, and sieve analysis. As well as the analysis of the ability of the stream to mobilize the bed material, by estimating the critical stream power. The goal of meeting these objectives is to illustrate the impacts of thermokarst activity on a MDV stream, and investigate the response of the stream.

Figure 2. Overview of Fryxell Basin. Highlighting Crescent stream East and West Branches (imagery courtesy of Polar Geospatial Center).

2. METHODS

2.1. Terrestrial LiDAR Scans

TLS Data Collection and Processing

When the thermokarst activity was discovered on the West Branch of Crescent Stream in January of 2012, the most heavily impacted area was documented with terrestrial LiDAR scanning (TLS) using a Riegel VZ – 400. Subsequent TLS has been taken in the same location every year with the most recent scan in January of 2014. This technology works by sending out laser pulses to measure the location of the ground surface relative to the location of the instrument. It does this for millions of points in a complete circle around the instrument that can be tens of meters in radius. The resolution of points is chosen by the user and was on average 6000 points per square meter for these scans, while the higher resolution on the thermokarst feature itself was up to 10,000 points per square meter. Unfortunately, this technology is unable to penetrate water which resulted in low point density in the channel where water was present. Also, because this technology depends on laser returns from the ground surface, shadowing can occur behind large rocks and boulders. Scans were collected from different angles to avoid some of this shadowing.

UNAVCO provided all of the support in collecting and processing the terrestrial LiDAR data. The method used for LiDAR data collection was as follows. The instrument was set up on a fixed tri-pod at the first scan position. The scan position was chosen to maximize the area covered within the area of interest, while minimizing shadows caused by large rocks. For each scan there were six targets set out anywhere from 10m to 100m on tri-pods that were visible to the instrument. The target coordinates and elevations were recorded using a Trimble 5700 unit

with differential GPS technology. These targets were used later in the data processing to geo-reference the scans. With all of the target locations recorded, and the scan completed, the instrument and targets were moved to the next scan position. The next scan position was then chosen to eliminate any shadowing that may have been a problem in the previous scan, as well as to capture more of the area of interest. This process was repeated until the entire area of interest was captured.

The data was processed by UNAVCO using the RiSCAN Pro software. The software is able to correlate many scans together using the target positions to geo-reference the point locations. For consistent analysis, the latitude and longitude of each point was converted into the Universal Transverse Mercator 58 South coordinate system and elevation of each point used the World Geodetic System 1984 as a datum.

TLS Point Cloud Registration

Upon receiving the data from UNAVCO, it was discovered that there was a need to register the original point clouds from the LiDAR scans to reduce the errors introduced by instrument error, GPS error, and geo-referencing errors. These errors were evident upon visual inspection of the point clouds in Cloud Compare, an open source point cloud analysis software used for this analysis. For points in areas where no geomorphic change would be expected, i.e. large boulders not in immediate vicinity of thermokarst activity, the 2013 data exhibited a vertical offset of about 5 cm, while the 2012 data had no noticeable difference aside from random noise. There is no way to determine which point cloud most accurately represented the true ground surface, however 2014 was arbitrarily chosen as the reference point cloud. That is,

for the registration the locations of points in the 2012, and 2013 point clouds were adjusted relative to corresponding points from the 2014 point cloud. The registration algorithm used in the Cloud Compare software utilizes the "Iterative Closest Point" algorithm by Besl and McKay (1992). This algorithm keeps the reference cloud fixed, while the other cloud is transformed to match the reference by iteratively applying a transformation matrix and minimizing a local mean-square distance metric of randomly sampled points.

To make sure that the registration was not being influenced by the true geomorphic change occurring, the points in the immediate vicinity of the thermokarst feature were not included in the registration. This was done by filtering out points in each survey that were found to be greater than a set distance apart. This process effectively removed the points in areas of true geomorphic change, and included only the points which represent a static ground surface for registration. The limit set for this distance was chosen based on the known instrument error of 0.6 cm, and the fact that the 2013 and 2014 offset was already about 5 cm. The values used to filter the points were 3 cm, and 8 cm for 2012 registered to 2014, and 2013 registered to 2014 respectively. To test the validity of the registration, the absolute value differences were calculated before and after registration and the mean values were calculated. It should be noted that these differences were calculated from the point clouds that exclude the points in areas of actual geomorphic change.

Table 1. Registration validation. Differences between filtered point clouds before and after registration

	Mean Difference (cm)	Standard Deviation (cm)
2012 - 2014		
Unregistered	1.3	0.7
Registered	1.2	0.7
2013 - 2014		
Unregistered	4.3	1.5
Registered	1.6	1.2

After registration, the point clouds were exported to ArcMap [*ESRI*, 2012] and converted to digital elevation models (DEMs) to allow for DEM differencing analysis. This was done using the "ArcGIS LAS Dataset to Raster (Conversion)" tool. The point to DEM conversion used natural neighbor interpolation with a 1 cm by 1 cm grid cell size resolution. Natural neighbors interpolation was used because it has been found to be the most efficient and accurate interpolation technique for LiDAR derived DEMs [*Bater and Coops*, 2009]. However, as with any interpolation technique, this interpolation method introduces error to the DEM. This is done by causing some of the higher resolution to be lost, and by interpolating surfaces over areas of low point density.

The DEM differencing analysis was conducted with the Geomorphic Change Detection (GCD) software plugin for ArcMap developed by Joe Wheaton (2015). This software is explained thoroughly in the paper by Wheaton et al. (2009). The method calculates the difference in elevation between two DEMs at each 1 cm by 1cm raster cell. The output is a single raster called a DEM of Difference (DoD) with raster cell values that represent the calculated difference between the two survey DEMs. This output DoD is then used to produce useful statistics like the volumes and areas of the landscape that has experienced erosion and deposition. Due to inherent uncertainties involved in the survey collection and processing, the

resulting DoD also has uncertainties associated with it. The GCD software includes a couple of different methods that were used to address the uncertainty in the DoD.

DEM of Difference Uncertainty Analysis

Minimum Level of Detection

One of the most common and simplest methods used for managing the uncertainties in a digital elevation model is to use a minimum level of detection (minLoD) (Wheaton et al., 2009). Where calculated elevation differences that fall below this minLoD are considered too low to detect and calculated differences that are found to be above this limit are considered to be real. This method owes its benefits and drawbacks to its simplicity. The method is easy to implement because it applies a spatially uniform uncertainty to the entire survey. However, in reality the uncertainty of the survey is a function of different factors such as the slope and roughness of the terrain, and the survey point density [*Barnhart and Crosby*, 2013]. A negative consequence of using this method is the loss of valid information. That is, true changes measured below this level of detection may be discarded as errors. Also, this method does not address the uncertainty in areas of low point density where inaccurate surfaces have been interpolated.

The minimum level of detection value is chosen based on the uncertainties associated with the instrument, geo-referencing and registration of the survey data. Based on the greatest mean error between surveys of 1.6 cm the minLoD and observing the results, the minLoD was originally chosen to be 3 cm. However, this resulted in a lot of noise in areas of low point density such as shadows, and areas with water. To investigate which minLoD was most suitable

for this application, a sensitivity analysis was performed by increasing the minLoD and observing the changes in the surface area of change, and the volume of change calculated.

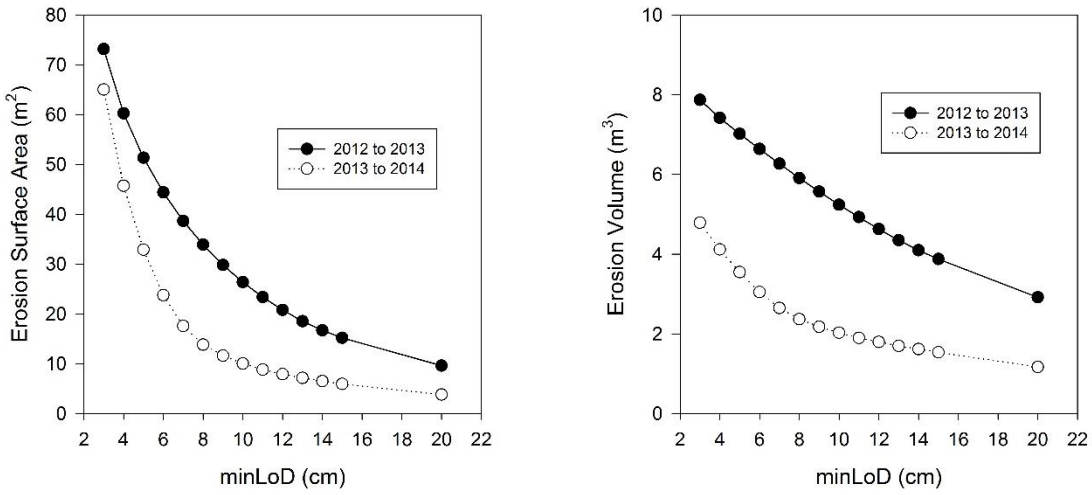

Figure 3. Plots of erosion surface area and volume plotted against minLoD (minimum level of detection).

Figure 3 shows the relationships between altering the minLoD and the corresponding changes in the erosion surface area and volume. The curves follow the same trend with decreasing values in area and volume with increasing minLoD values. However, the relationship between the minLoD and the erosion surface area plot is most informative. The resulting false differences which are manifested in the Raw DoDs have a significant surface area when compared to the surface area of the true differences (Table 4). However, the volumetric differences between the Raw DoD and the minLoD DoD are less substantial. This is because the false differences are typically small changes in ground surface and do not account for much total volume, while the true differences can be on the order of 0.5 m and thus account for a significant total volume.

The linear trends seen from 3 cm to 6 cm in both years of data on the surface area plot represent the removal of the false differences. The surface area decreases significantly with only

one centimeter increments in the minLoD. At minLoD values larger than 6 cm the trend begins to flatten out. This is the result of having removed the majority of the false differences, while beginning to steadily remove the true differences at higher values. The relationship between the area of change and the minLoD along with visual inspection of the DoD maps resulted in an optimal minLoD of 10 cm.

Fuzzy Inference System

The spatially uniform minLoD is a relatively simple approach to dealing with the uncertainty of the DoD, and thus a more intensive approach was considered to attempt to compute a more accurate DoD. A more thorough approach in dealing with the uncertainty of a DoD is to vary the minLoD spatially as informed by input variables. The GCD plugin allows for this by utilizing a Fuzzy Inference System (FIS) to create an error surface. The FIS works by relating inputs values to output uncertainties using linguistic adjectives. A thorough description of how a FIS works in this context can be found in Wheaton et al. (2009). The inputs used for the FIS in this analysis were slope and point density rasters created with the GCD tool. These were chosen as the two input variables of interest because of the influence slope and point density can have on DEM uncertainty. The input to output relationships were developed based on the known inherent error of the surveys, as well as the reasoning that point density and uncertainty are inversely related, while slope and uncertainty have a direct relationship. Membership limits for the adjectives were developed based investigating the histograms of the inputs and measured differences from the DoD. Figure 4 illustrates the limits used for the membership of each input and output. Table 2 then shows the resulting uncertainty for all possible combinations of the two input variables. Using the GCD tool and these rules, spatially

variable error surfaces were created for each survey DEM. These error surfaces were then used to calculate the DoD with a 95% confidence limit on the calculated differences.

Table 2. Membership rules for fuzzy inference system used to determine DoD uncertainty

FIS Relationship Rules		
Inputs		**Result**
Slope	*Point Density*	*Elevation Uncertainty*
Low	Low	High
Low	Medium	Average
Low	High	Low
Medium	Low	Extreme
Medium	Medium	Average
Medium	High	Low
High	Low	Extreme
High	Medium	High
High	High	Average

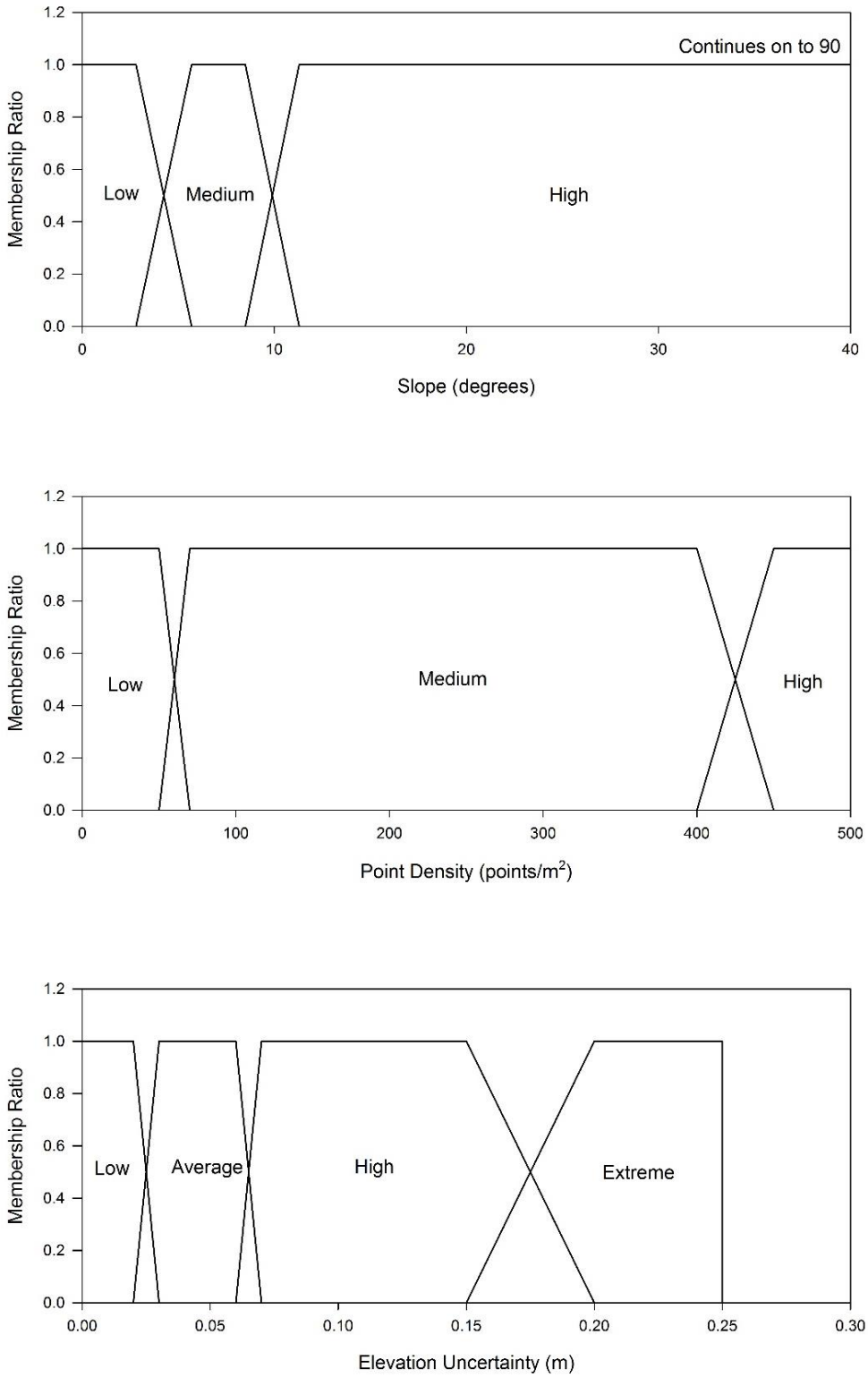

Figure 4. Plots of FIS system showing membership ratios and values that define each category

2.2. Sediment Data

Sediment Sampling

In January of 2015, sediment data was collected to investigate the impacts of the thermokarst activity on the sediment size distribution of the west branch of Crescent Stream. The three methods used in this investigation to characterize the sediment were fine sediment counts, pebble counts, and sediment sieving.

Fine Sediment Counts and Pebble Counts

The fine sediment counts and the pebble counts were performed on reaches throughout both branches of Crescent Stream (See Figure 5 for specific locations). Both methods used the same setup which was informed by the work of Bunte & Abt (2001). The reaches sampled were 50 m reaches measured by laying out a tape along one side of the stream, following the planform of the stream. Each reach was sub-sampled at 11 cross sections spaced 5 m apart. At each cross section a tape was laid across the channel perpendicular to the stream flow. The cross sections were then sub-sampled at set intervals typically 5 or 10 cm based on the width of the wetted stream channel. At each sample interval along the cross section, one person would drop a thin vertical rod 1mm in width and note the grain of sediment that was struck first by the rod. This is the step where the two sampling methods deviate.

Fine Sediment Counts

For the fine sediment counts, if the rod hit a grain of sediment that was visually confirmed to be less than 2 mm the sampling partner recorded a "yes" for fine sediment, if the rod hit a grain of sediment greater or equal 2 mm the sampling partner recorded a "no" for fine sediment. This method is similar to a traditional pebble count, however allows for more rapid measurements to be taken because the sediment grains do not have to be removed and measured by hand. This efficient method was adopted to allow for greater spatial sampling within limited time constraints, while still providing adequate data to assess the impact of the thermokarst features on the distribution of fine sediment throughout the West Branch.

The fine sediment counts were analyzed by producing maps of each reach to illustrate the difference in fine sediment distributions on the east and the west branches. Each cross section was represented by a row of rectangles that was scaled to the measured width at that location. Each rectangle represents a single measurement location, and each location was colored according to the fine surface material measurements. A fine material measurement was denoted by a light gray color, while a coarse material measurement was given a dark gray color. These cross sections were then stacked on top of each other with the furthest upstream cross section at the top of the plot, and the furthest downstream cross section at the bottom of the plot. The cross sections are actually 5 m apart in reality, however for simplicity they were plotted directly adjacent to one another.

The fine sediment counts were also summarized in a single plot. For this plot the average percent fine was calculated for each reach (i.e., average of all eleven cross sections) and plotted against the location of the reach relative to the gaging station. The average percent fine of each reach was calculated by taking the percent fine for each of the eleven cross sections within the

reach and calculating an un-weighted average of the percentages. The percent fine values were then given error bars to represent the standard deviation of the eleven averaged percent fine values of each reach.

Pebble Counts

For the pebble count method, the specific grain that was struck by the rod first was then picked up, measured with calipers, and recorded by the sampling partner. The intermediate axis of each sediment grain is the dimension that was measured for each particle. This is a much more time consuming sampling method when compared with the fine sediment count method. However, this method allows for a much more thorough understanding of the distribution of bed material sediment sizes.

The pebble counts were analyzed by grouping the particle sizes into bins to obtain the size distribution of the particles. The bin values were selected based on the sediment size classifications for sands, gravels, and cobbles (Table 3). The distributions of each pebble count were then illustrated by plotting the cumulative fraction of particles, by number, that were measured to be smaller than each partition value. The representative particle diameters D_{16}, D_{50}, and D_{84} were also calculated for each pebble count.

Table 3. Sediment size classes used to bin pebble count results. (Modified from Bunte & Abt, 2001)

Size (mm)	Description of Particle Size	
1024		
	Medium	
512		Boulder
	Small	
256		
180	Large	
128		Cobble
90	Small	
64		
45	Very Coarse	
32		
22	Coarse	
16		
		Gravel
11	Medium	
8		
6	Fine	
4		
	Very Fine	
2		
	Very Coarse	Sand

Sieve Sampling

The sediment samples that were collected for the sieve analysis were only collected at two of the 50 m reaches. One reach located on the East Branch (East 2) and the other on the West Branch (West 2) (Figure 5). The reach on the West Branch was chosen because it is located in the midst of the most significant thermokarst activity and was covered by the TLS. The reach on the East Branch was chosen because it was located at a similar distance upstream with a similar slope to the reach on the West Branch, thus allowing for more acceptable comparison between the two branches. Each reach was sub-sampled at five cross sections each spaced 10 m apart. These were the same cross sections sampled in the pebble counts, however every other cross-section was skipped.

At each cross section three characteristic areas were visually defined by looking at the surface material. Within the wetted stream channel, locations of fine material and coarse material were defined. Outside the channel, one location of the bank material was defined. This resulted in three characteristic areas per cross section fine material, coarse material, and bank material. Within each characteristic area, two sediment samples were taken. The first sample was the surface material which collected all sediment particles down to a depth of about 2 cm, and the second sample was taken in the same exact location as the surface material and collected sediment down from about 2 cm to 8 cm. The average sample was around 80 grams, which is relatively small for a sediment sample size. However, the samples were hiked back to a field camp, then flown by helicopter back to McMurdo for sieve analysis, which limited the weight of samples that could be taken.

After collection and transport back to the lab, these samples were baked in a lab oven at 50°C for 24 hours to ensure all water was evaporated from the sample. This is an important step

to ensure that the mass of the sediment measured by the scale doesn't include any water. The sieve set was comprised of the following sizes: 0 mm, 0.25 mm, 0.5 mm, 1 mm, 2 mm, 3 mm, 4 mm, 6.3 mm, 12.7 mm, and 25.4 mm. This sieve setup was designed to follow the 0.5ϕ unit spacing as close as possible, however it was largely dictated by which sieves were available for use. Before each sieving, each individual sieve was weighed. The dried sediment was then poured into the sieve set, and the sieve set was shaken using an automated sieve shaker for one minute. The sieves were individually removed, weighed, and recorded. The mass of the empty sieve was subtracted from the mass of the sieve plus the retained sediment, resulting in the mass of the retained sediment.

The sieve data were illustrated using a couple of different methods. The first method was created to show how the sediment size of each sieve sample changed along the reach while also comparing the East and West Branches. For example the first of these plots illustrated the surface fine material of each branch. The D_{50} of each sieve sample was plotted on the x-axis, with error bars that represented D_{16} and D_{84} on the lower and upper bounds respectively. These points were plotted in pseudo space on the y-axis with the plot representing a view of the reach from above. The highest point on the y-axis represents the furthest upstream sample location of the reach. This plot was created for each type of sieve sample taken resulting in six plots all together.

The second method used for illustrating the sieve data was to group the samples into representative groups and plot the fraction passing each sieve size. The representative groups were surface material, and sub-surface material for each branch. Each representative group then has three sub-groups which are bed coarse material, bed fine material, and bank material. Each sample was collected and sieved separately, however for this method these measurements were

grouped together as if they were combined and sieved as one sample. This was accomplished by combining all 5 of the samples of a sub-group, for example west branch surface fine material. The samples were combined by summing the mass retained on one sieve size for all 5 samples, repeating this for each sieve size, and then analyzing it as if it were one large sample.

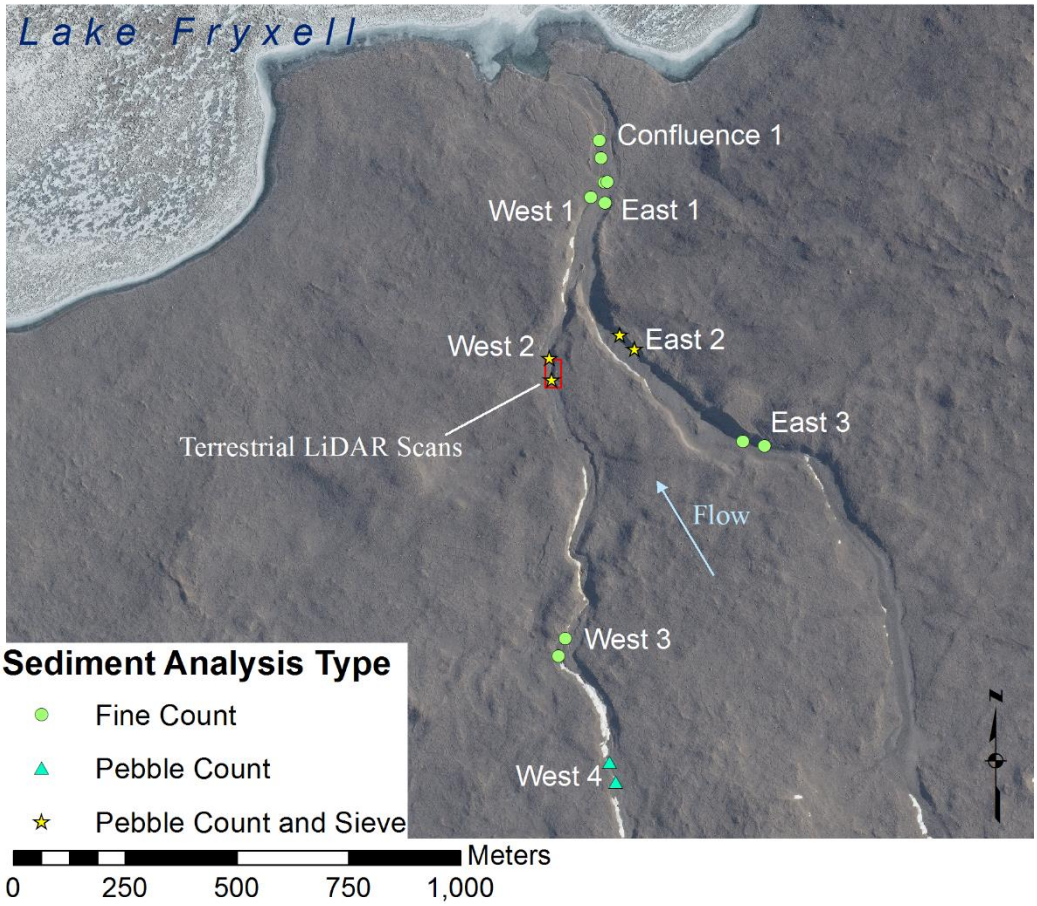

Figure 5. Map of sample types and locations. Each point represents upstream and downstream limits of sample reach.

2.3. Stream Power

Critical Stream Power

In investigating the impacts of the thermokarst on Crescent Stream, it was of interest to consider the ability of the stream to mobilize the sediment within the channel. With the LiDAR scans there exists extremely high resolution surveys of the channel geometry in certain locations. However, because of the low flows experienced in the 2014-2015 season, very little hydraulic data was collected. The flow depth, velocity, and flow rate measurements that are necessary for verifying hydraulic models, and informing sediment transport equations were not collected. Stream power is a useful metric to investigate sediment mobilization capabilities using only gross channel parameters. The unit stream power is defined as

$$\omega = \rho g Q S / w \qquad (1)$$

Where Q denotes the flow rate, ρ represents the density of water, g is the acceleration of gravity, S denotes the slope of the channel, and w represents the channel width. This equation represents the mean value of stream power per unit bed area.

Bed-load transport in gravel bedded rivers occurs at a very low rate until a threshold flow rate is reached. After this threshold, transport rates increase non-linearly [*Ferguson*, 2005]. Knowledge of this threshold value is useful in addressing the transport capacity of gravel bedded rivers. Bagnold (1980) proposed a formula to calculate the critical stream power necessary to transport a bed described by a characteristic particle size, D.

$$\omega_c = c_1 D^{1.5} \log(c_2 h / D) \qquad (2)$$

Where ω_c is the critical stream power, c_1 and c_2 are constants, D is the diameter of the characteristic particle size of the bed, and h is the mean flow depth. This equation has a couple of disadvantages. In this form, Eq. (2) still requires knowledge of the flow depth h, and values for c_1 and c_2 are given without full explanation as to what they represent. Conveniently, Ferguson (2005) pointed out these concerns, and derived a new set of equations to calculate the critical stream power needed to mobilize a gravel bed.

The detailed derivation of the equation used in this analysis can be found in Ferguson (2005). He proposes two different equations that differ in the form of flow resistance used. He proposes one in the form that utilizes the logarithmic flow resistance law as used by Bagnold, as well as an equation that utilizes the Manning-Strickler flow resistance relation. The equation which utilizes the Manning-Strickler relation was chosen for this application. The Manning-Strickler flow resistance relationship is most appropriate for applications where flow resistance is caused entirely by grain roughness, which is a valid assumption for this scenario. So, Ferguson's full critical unit stream power is used here.

$$\omega_{ci} = a\rho(\theta_{cb}RgD_b)^{\frac{3}{2}}\left(\frac{\theta_{cb}R}{S}\right)^{\frac{1}{6}}\left(\frac{D_i}{D_b}\right)^{5(1-b)/3} \qquad (3)$$

[*Ferguson*, 2005]

Where a is a constant from the Manning-Strickler relation with a value of 8.2, D_b is a representative particle diameter for the bed surface material responsible for the flow resistance, θ_{cb} represents the dimensionless Shields stress for entrainment of particles size D_b, R denotes the submerged specific gravity, D_i denotes the representative particle size of the bed and b is the hiding factor with a value between 0 and 1.

This form of the critical stream power equation is much more easily applied in this application when compared with Bagnold's original equation Eq. (2). It allows for the critical stream power to be solved for without the need for a flow depth. This equation uses only the slope of the channel, and the distribution of the bed surface material. The sediment size distribution values have been calculated in previous steps. The only information that remains unknown in Eq. (3) is the slope of each reach.

Estimating Slope

For all sample reaches that were included in the 2015 LiDAR scans, the slopes were calculated from the TLS data. This included reaches West 1, West 2, East 1, East 2, and East 3. In this case a line was traced along the thalweg of the channel in ArcGIS. Using the "Stack Profile" tool the elevations along the line were extracted from the 2015 DEM and converted into a table of horizontal distances, and elevations. A linear trend line was fit to each reach and the slope of the trend line was taken to be the slope of the sample reach.

For reaches that were outside of the 2015 terrestrial LiDAR scans the slopes were calculated using the 2001 aerial 2m resolution LiDAR scan of Taylor Valley [*Schenk et al.*, 2004]. It should be noted that the landscape has changed since 2001 as documented above. However, the slope adjustment of the stream since 2001 is assumed to be minor. First, the DEM was brought into ArcGIS and the points that were manually surveyed were dropped onto the DEM to determine the exact location of the beginning and ending of the sample reaches. Using the hydrology tools of ArcMap the East and West Branches of Crescent stream were delineated. The location of the stream channel was not always in perfect alignment with the surveyed reach

points because of channel migration since 2001, and inaccuracies in the DEM. The elevations along the stream channels were extracted from the 2001 DEM and written to a table using the "Stack Profile" tool in ArcMap. Linear trend lines were fit to each reach and the slope of the trend line was taken as the slope of the reach.

The slope of the channel along the entire stream network was also estimated and plotted. This process used the same stream delineation and DEM from the 2001 aerial LiDAR data. The table of extracted distances and elevations was sampled at 20m increments along the stream network. The slope at every 20m increment was calculated by taking the difference in the elevation of the current point and the next point upstream divided by the difference in distance between the two points. This yielded a table full of average slopes every 20m for the entire channel network. A 5 cell wide moving average was used to smooth the data while still capturing the true variability in slope. The smoothing algorithm dealt with the ends of the slope vector by taking the average of whatever is available. For example given the slopes $[S_1, S_2, S_3, S_4, \dots S_n]$ the following shows the calculations of the smoothing algorithm.

$$S_{1_{smoothed}} = S_1$$

$$S_{2_{smoothed}} = \frac{S_1+S_2+S_3}{3}$$

$$S_{3_{smoothed}} = \frac{S_1+S_2+S_3+S_4+S_5}{5}$$

The 100m reach average slope was then plotted on the y-axis with the distance upstream on the x-axis. The slopes determined for each reach using the previous mentioned methods were also plotted as points in their respective locations to validate their accuracy.

Flow Probability on Crescent Stream

With the slopes and the sediment size distributions of the bed material known, the critical stream power of each reach of interest can be calculated, however this value is not very useful unless compared with potential stream powers that Crescent Stream may potentially experience. Every variable is known in the stream power equation Eq. (1) except for the discharge. Crescent stream has been gaged since 1990 and the data are available up to 2013. The station measures the stage at 15 minute intervals, and the stages are later converted to discharges using a stage discharge relationship that has been developed. The flow record is fairly complete, however there are some major gaps in the data after the gage was inundated with sediment in January 2012 coincident with the thermokarst activity. Since that time, the gaging has resumed, though a quality stage-discharge relationship has yet to be established. Nevertheless, there are over 41,000 fair to high quality (as noted in the dataset) recorded discharges that were used for analysis [*McKnight*, 2014].

The two branches of Crescent Stream are not gaged individually. The long-term gage site is located downstream of the confluence of the two branches. During the 2014-2015 season an attempt was made to estimate the flow contribution of each branch so that previous flow measurements could be separated into two flows. Pressure transducers were placed within the stream in each branch, and flow measurements were taken using a Baski Flume to establish stage discharge relationships. However, the flows were extremely low and any small variability in flow was unmeasurable with the Baski. The Baski measurements on each branch were consistently very similar, which suggests that the two branches contribute similar amounts of flow. Also, on days when flow ceased on one branch, no flow was observed on the other branch. The sources of each branch is not the same, however the controls on flow are very similar

because of the similarity in the aspect of the glaciers that feed them. Without knowing the true flow contribution of each branch, the gaged flows were simply halved giving each branch equal contribution.

Due to the high inter-annual variability and the limited flow record, the traditional method of ranking the annual peak flows, and determining the X-year recurrence interval of flows was not appropriate for this analysis. Instead, all of the measured flows were collected into one large sample group and a flow duration curve was created. Only flows that were rated as "good" or "fair" were used in this analysis, and all flow measurements of zero were discarded. This flow duration curve was then used to inform the critical unit stream power equation.

Bed Material Mobilization Calculations

The representative particle size of a stream-bed, mobilized by a given stream power, can be solved for in the Ferguson equation Eq. (3). The critical stream power on the left hand side of Eq. (3) can be replaced with Eq. (1) as shown below.

$$\rho g Q S / w = a\rho(\theta_{cb} R g D_b)^{\frac{3}{2}} \left(\frac{\theta_{cb} R}{S}\right)^{\frac{1}{6}} \left(\frac{D_i}{D_b}\right)^{5(1-b)/3} \qquad (4)$$

Each percentile of flow as calculated in the previous section was plugged into Eq. (1), along with the slope of the reach of interest, and average width to create a distribution of stream powers with estimated probabilities of occurrence. The percentiles of flow used in this analysis were the maximum observed flow, 99, 98, 95, 90, 80, 70, 60, 50, 40, 30, 20, 10, 5, 2, and 1. The average width of each reach was calculated as the average width of the 11 cross sections within each reach. The widths were determined using the pebble count measurements which denoted the

right edge of channel and left edge of channel for each cross section. The known values of the right hand side of Eq. (4) were then populated. It is assumed that that $\rho = 1000\ kg/m^3$, $g = 9.81\ m/s^2$, $R = 1.65$, and $\theta_{cb} = 0.047$ (Figure 7.8 [*Julien*, 2010]). The constant $a = 8.2$ from the Manning-Strickler relation, and $b = 0.7$ for the grain hiding factor. The representative surface roughness diameter, D_b, values used were the D_{50}values calculated from the pebble counts. The consequence of needing the bed material size distribution means that this analysis could only be completed for reaches with pebble counts which were the West 2, West 4, and East 2 reaches. The only unknown remaining in Eq. (4) is the D_i term, which is the diameter of the particle size that represents the bed material transported by the given stream power. This diameter was solved for while varying the amount of stream flow. The results were plotted with the particle size diameter on the y-axis and the percentile of flow on the x-axis. The plots also include the D_{16}, D_{50}, and D_{84} for each analyzed reach for comparison.

3. RESULTS

3.1. Geomorphic Change Detection Results

The two geomorphic change detection analyses yielded very similar results as is apparent in Figures 6 and 7, and Table 4. There was significant erosion (negative change in ground surface elevation) on the order of 0.5 m measured on the East bank of the channel for both the 2012 to 2013 and the 2013 to 2014 analyses. Many of the areas of significant erosion show small amounts of deposition (positive change in ground surface elevation) on the order of 0.1 m just below the impacted areas.

The total volume of erosion from 2012 to 2013 was calculated to be around 5 m^3 which was more than double the 2 m^3 measured from 2013 to 2014. The volumes of deposition reported were much less than the volumes of erosion. The volume of deposition measured from 2012 to 2013 was only 0.29 m^3. The volume of deposition measured from 2013 to 2014 had disagreement between the two methods used, however the values averaged out to 0.24 m^3, which was very similar to the 2012 to 2013 value. The average depths of erosion from 2012 to 2013 and from 2013 to 2014 were about the same with values around 0.2 m. The average erosion depths for the two years were also very similar with values around 0.1 m. The erosion and deposition values were significantly impacted by the uncertainty analysis. This is seen by comparing the raw values to the minLoD 10 cm and FIS values in Table 4. The Raw erosion volume from 2012 to 2013 was cut nearly in half after the uncertainty analysis, and was reduced to less than half in 2013 to 2014. The deposition volumes were most significantly impacted being reduced from 3.79 m^3 to 0.29 m^3 in the 2012 to 2013 analysis, and from 2.73 m^3 to 0.24 m^3

in the 2013 to 2014 analysis. The areas of erosion and deposition were also reduced significantly.

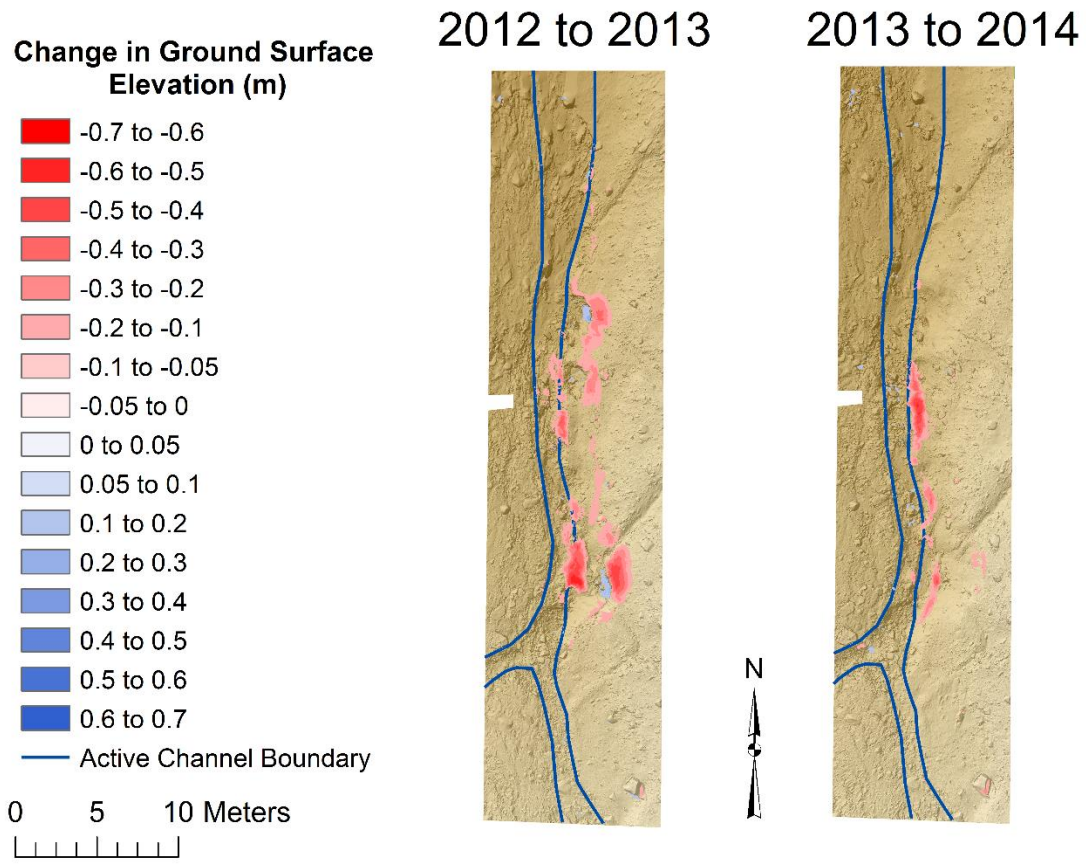

Figure 6. Change in ground surface over time. Side by side comparison of DEMs of difference using a minLoD of 10 cm on a thermokarst impacted area on the West Branch. Red coloring indicates areas of measured erosion (decrease in ground surface elevation), and blue coloring indicates areas of measured deposition (increase in ground surface elevation).

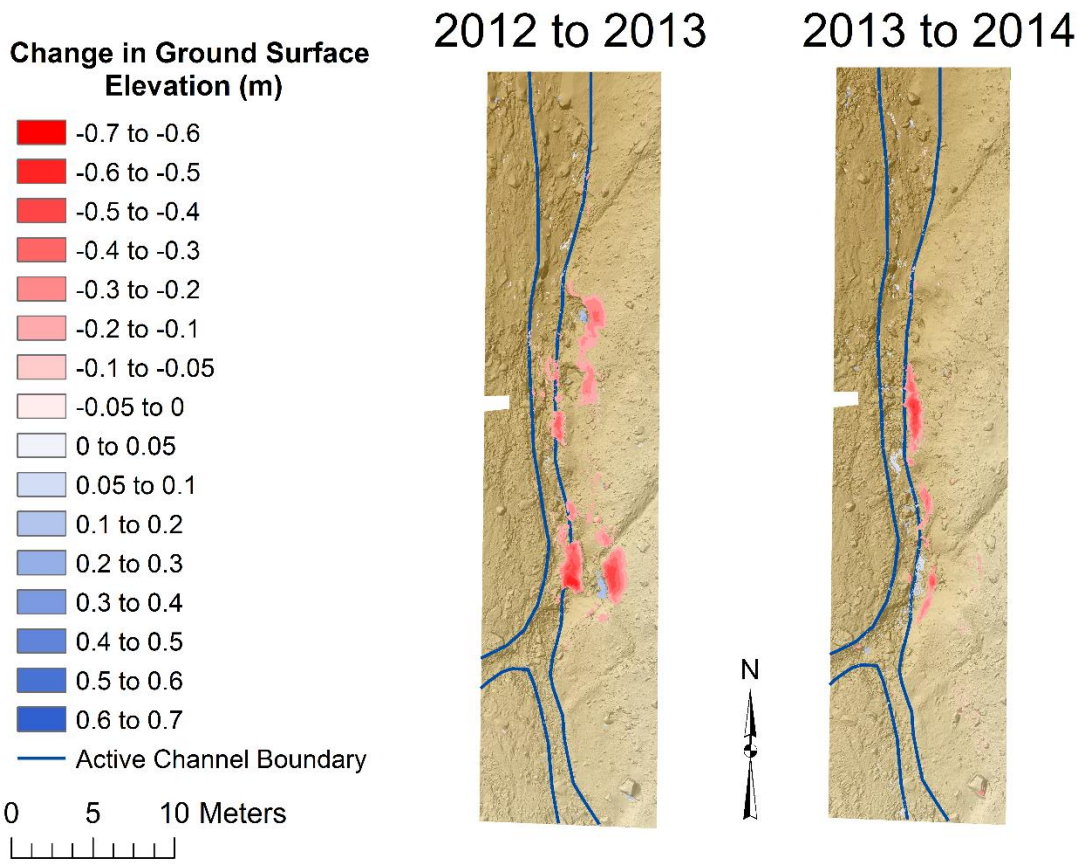

Figure 7. Change in ground surface over time. Side by side comparison of DEMs of difference using a FIS on a thermokarst impacted area on the West Branch. Red coloring indicates areas of measured erosion (decrease in ground surface elevation), and blue coloring indicates areas of measured deposition (increase in ground surface elevation).

Table 4. Results from the DEM of Difference analysis. Red values indicate erosion (decrease in ground surface elevation), and blue values indicate deposition (increase in ground surface elevation).

	2012 - 2013			2013 - 2014		
	Raw	min LoD 10cm	FIS	Raw	min LoD 10cm	FIS
Erosion Volume (m^3)	9.18	5.24	4.68	7.2	2.03	1.9
Error Volume (m^3)	-	2.64	1.36	-	1.01	0.58
Deposition Volume (m^3)	3.79	0.29	0.29	2.73	0.16	0.31
Error Volume (m^3)	-	0.2	0.16	-	0.12	0.41
Area of Erosion (m^2)	209	26.4	22.5	311	10.1	10.5
Area of Deposition (m^2)	287	1.98	2.81	185	1.24	4.51
Average Depth of Erosion (m)	0.04	0.2	0.21	0.02	0.2	0.18
Average Depth of Deposition (m)	0.01	0.15	0.1	0.01	0.13	0.07

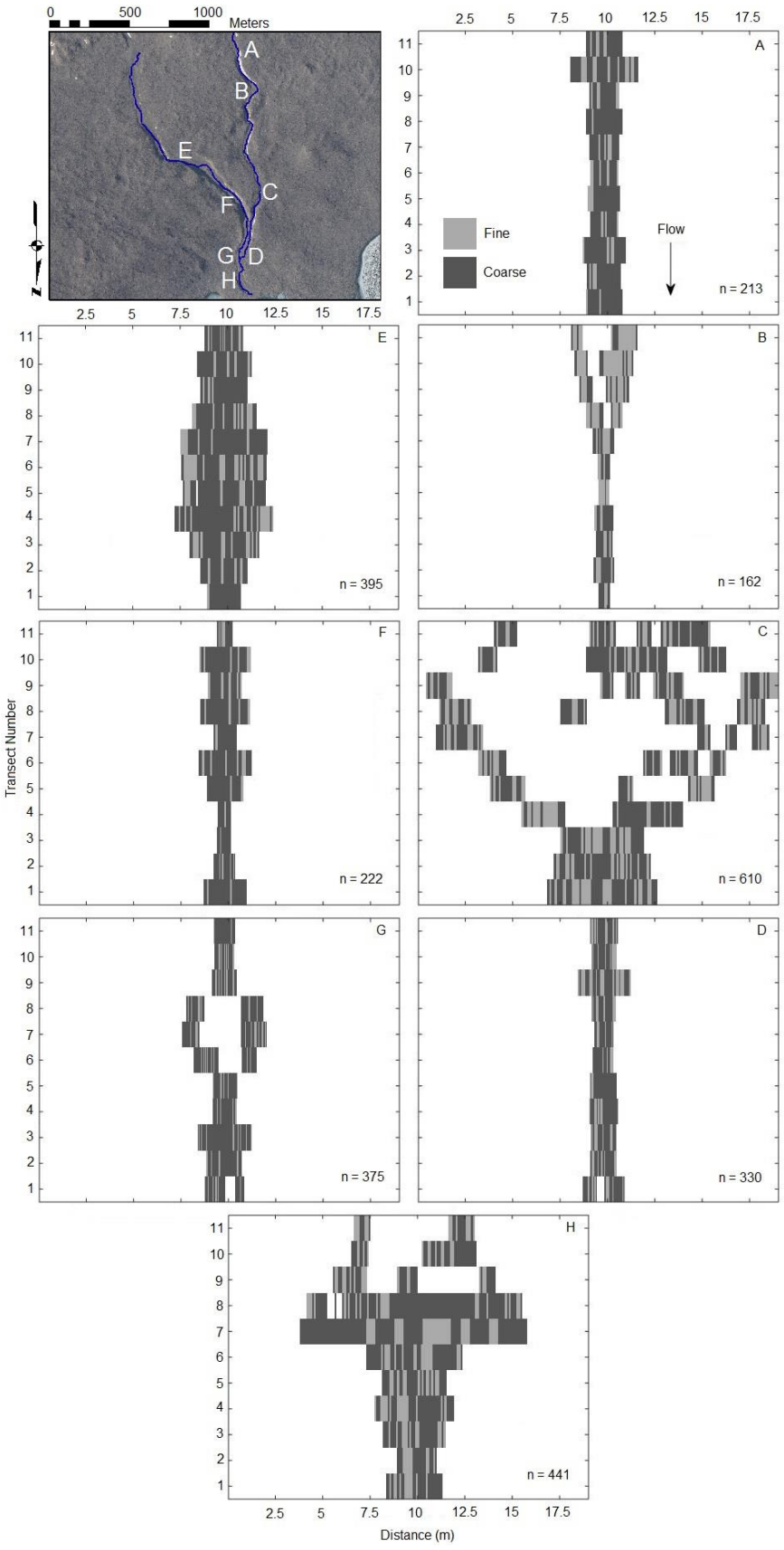
0
500
1000
Meters
A
B
C
D
E
F
G
H
N
Fine
Coarse
Flow
n = 213
n = 395
n = 162
n = 222
n = 610
n = 375
n = 330
n = 441
Transect Number
Distance (m)

Figure 8. Qualitative maps of fine sediment counts. The top of the page is upstream and the bottom of the page is downstream. Left column is East Branch, right column is West Branch and the center is the confluence. A: West 4, B: West 3, C: West 2, D: West 1, E: East 3, F: East 2, G: East 1

3.2. Fine Count Results

The fine counts were illustrated using two different methods to look at the spatial distribution of fine sediment along both branches. The fine count maps (Figure 8) show that the West Branch reaches have a consistently higher percentage of fine measurements when compared to the corresponding East Branch reaches. This distinction is most prevalent when comparing the amount of light colored measurements in the East and West 3 reaches. The confluence map shows a significant number of fine sediment measurements when compared to the upstream East Branch. There were no noticeable spatial patterns of fine sediment distributions within any of the reaches.

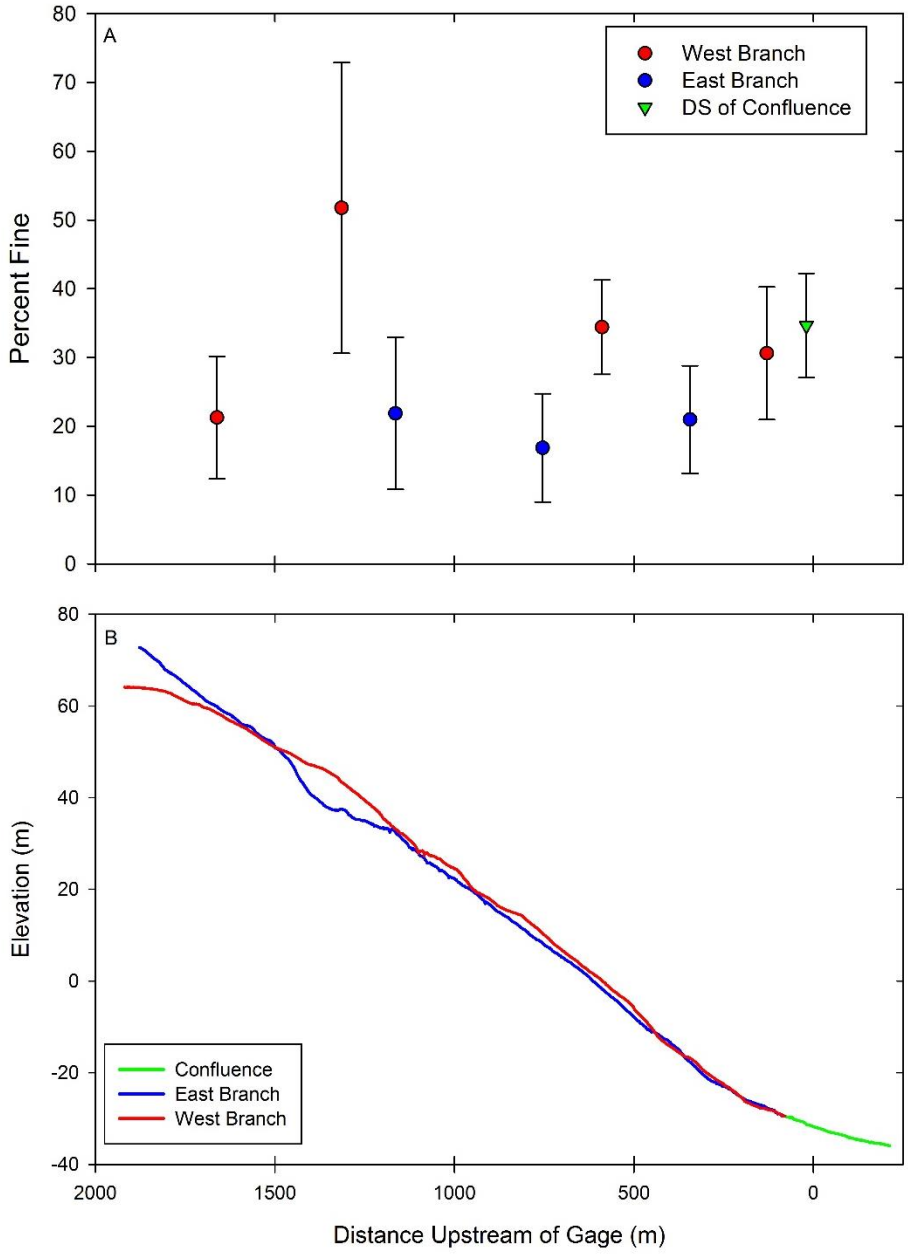

Figure 9. A: Reach average percent fine values plotted against the distance upstream of the gage. The error bars represent the standard deviation of the 11 cross-section percent fine values within each reach. **B**: Longitudinal profile of Confluence, East, and West Branches.

The plot of percent fine versus distance upstream shows the longitudinal distribution of fine sediment throughout the stream network (Figure 9 A). As shown in Table 5, the most upstream reaches of the East and West Branches (East 3 and West 4) were found to have very

similar average percent fine values of around 21%, and standard deviations of about 10%. Moving downstream along the West Branch, the percent fine value peaks at the next reach, West 3, with a value of 52% and a relatively large standard deviation of about 20%. The percentages decrease gradually from 34% at West 2, and then to 31% at West 1.

Moving downstream on the East Branch the percent fine values remain relatively constant. The average percent fine dips slightly to 17% at East 2, and then back up to 21% at East 1. The confluence value for the average percent fine was found to be significantly larger than all East Branch values and similar to the lower two West Branch values at 35%. The longitudinal profile of each branch was also included for context. The slope of the East Branch becomes very gradual just upstream of East 3, and the slope of the West branch also becomes very gradual just upstream of West 4 (Figure 9 B).

Table 5. Summary of percent fine values, slopes, and distances upstream of gage for each reach.

Reach	Distance Upstream From Gage (m)	Slope (m/m)	Percent Fine (%)	Standard Deviation Percent Fine (%)
W04	1661	0.048	21.3	8.9
W03	1314	0.042	51.7	21.1
W02	589	0.065	34.4	6.9
W01	130	0.035	30.6	9.6
E03	1164	0.076	21.9	11.0
E02	754	0.060	16.9	7.9
E01	344	0.024	21.0	7.8
C01	20	0.030	34.6	7.6

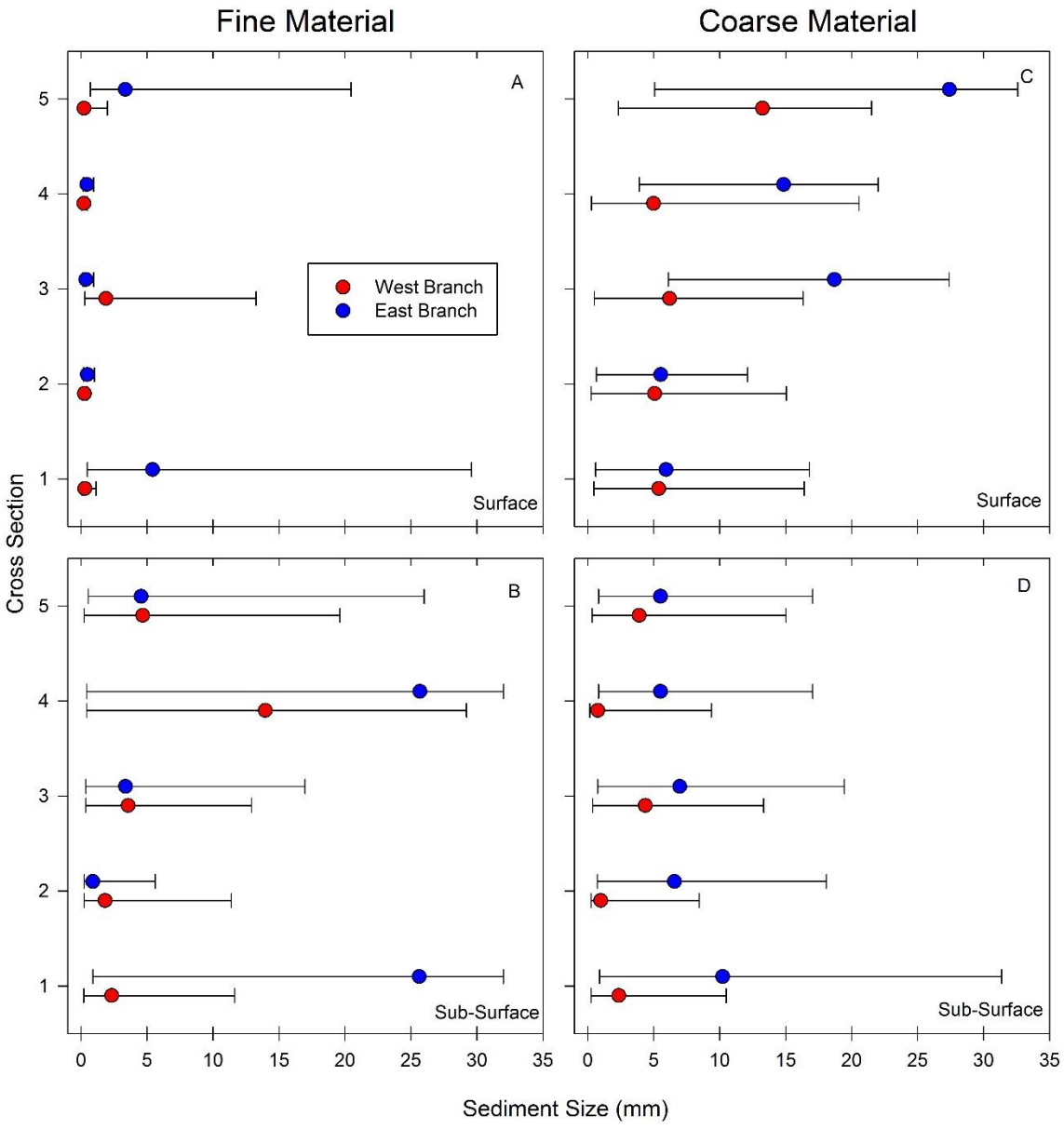
Fine Material
Coarse Material
A
B
C
D
West Branch
East Branch
Surface
Sub-Surface
Cross Section
Sediment Size (mm)
0
5
10
15
20
25
30
35
1
2
3
4
5

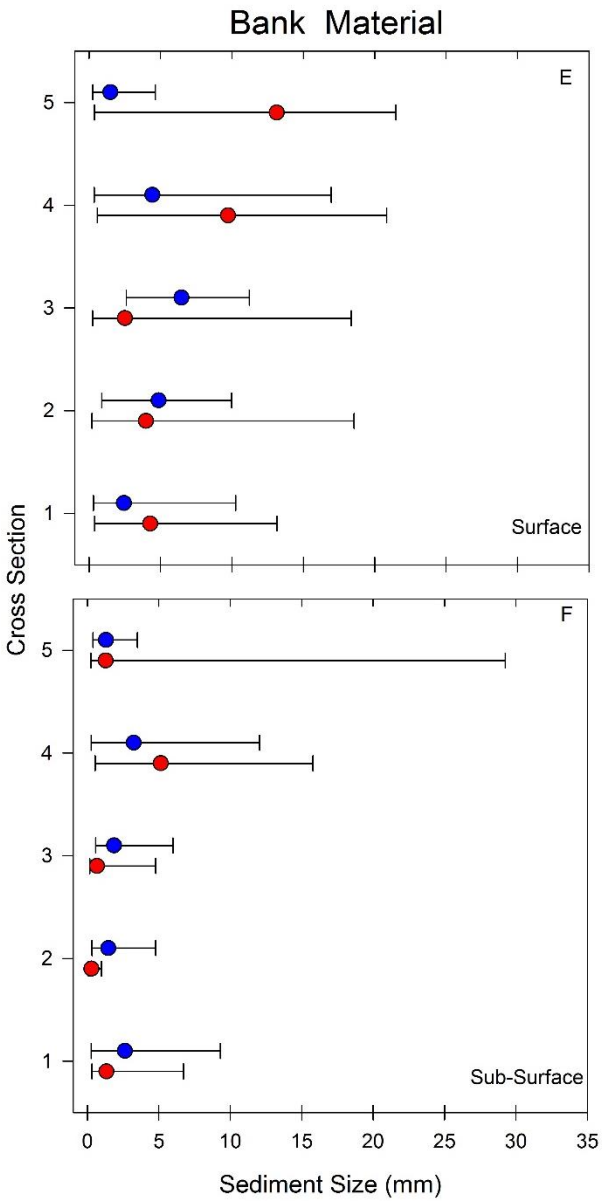

Figure 10. Sieve analysis results separated by branch, cross-section, and sediment sample location type. The center colored dots represent the $\mathbf{D_{50}}$ values, while the error bars represent the $\mathbf{D_{16}}$ and $\mathbf{D_{84}}$ values. The cross sections are organized such that cross-section 5 is upstream and 1 is downstream, each cross-section is spaced 10 m apart. A: Fine Material Surface, B: Fine Material Sub-Surface, C: Coarse Material Surface, D: Coarse Material Sub-Surface, E: Bank Material Surface, F: Bank Material Sub-Surface.

3.3. Sieve Sample Results

The fine material surface samples for the West Branch showed consistently tight distributions with D_{16} and D_{84} values that did not deviate far from the D_{50} value (Figure 10). The East Branch fine surface distribution had more variation in the distributions. There was no significant trend present when comparing the fine material surface distributions of the East and West Branches. The Fine material sub-surface sample D_{50} values were found to be larger than the fine material sub surface D_{50} values, and the range of sediment sizes tended to be larger as illustrated by the range of the D_{16} and D_{84} error bars. The East Branch coarse material surface and sub-surface D_{50} values were found to be consistently greater than the West branch values. The bank material sub-surface samples were found to be finer and less variable than the bank material surface samples.

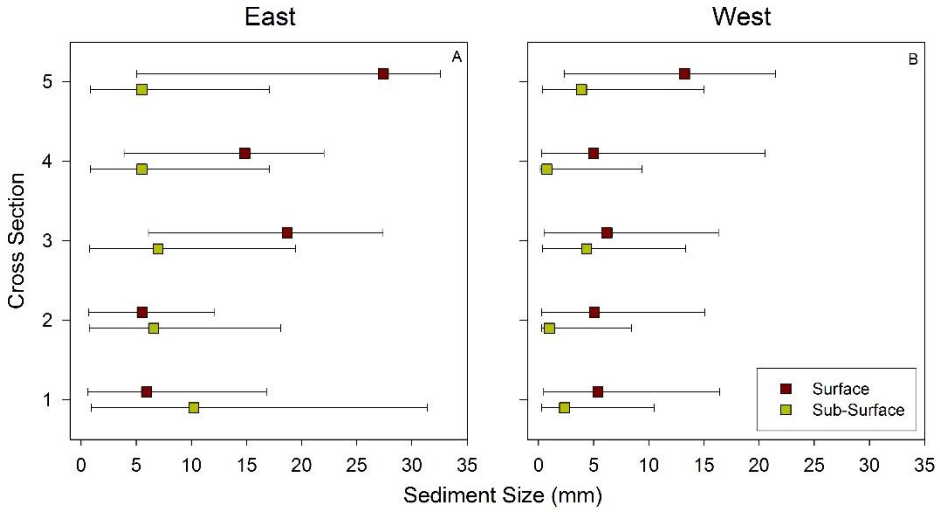

Figure 11. Coarse bed material armoring plot comparing the coarse material surface and sub-surface samples of both the East 2 and West 2 reaches. Cross section 5 is upstream and 1 is downstream, each cross-section is located 10 m apart. **A:** East 2 coarse material surface and sub-surface, **B:** West 2 coarse material surface and sub-surface.

It appears that for the coarse samples on both branches the sub-surface material tended to be finer than the surface material, a phenomenon known as bed armoring. A more thorough look

shows that for three of the five cross sections on the East Branch, the sub-surface material was finer than the surface material (Figure 11). On the West Branch, all five sub-surface measurements had finer D_{50} values than the surface measurements.

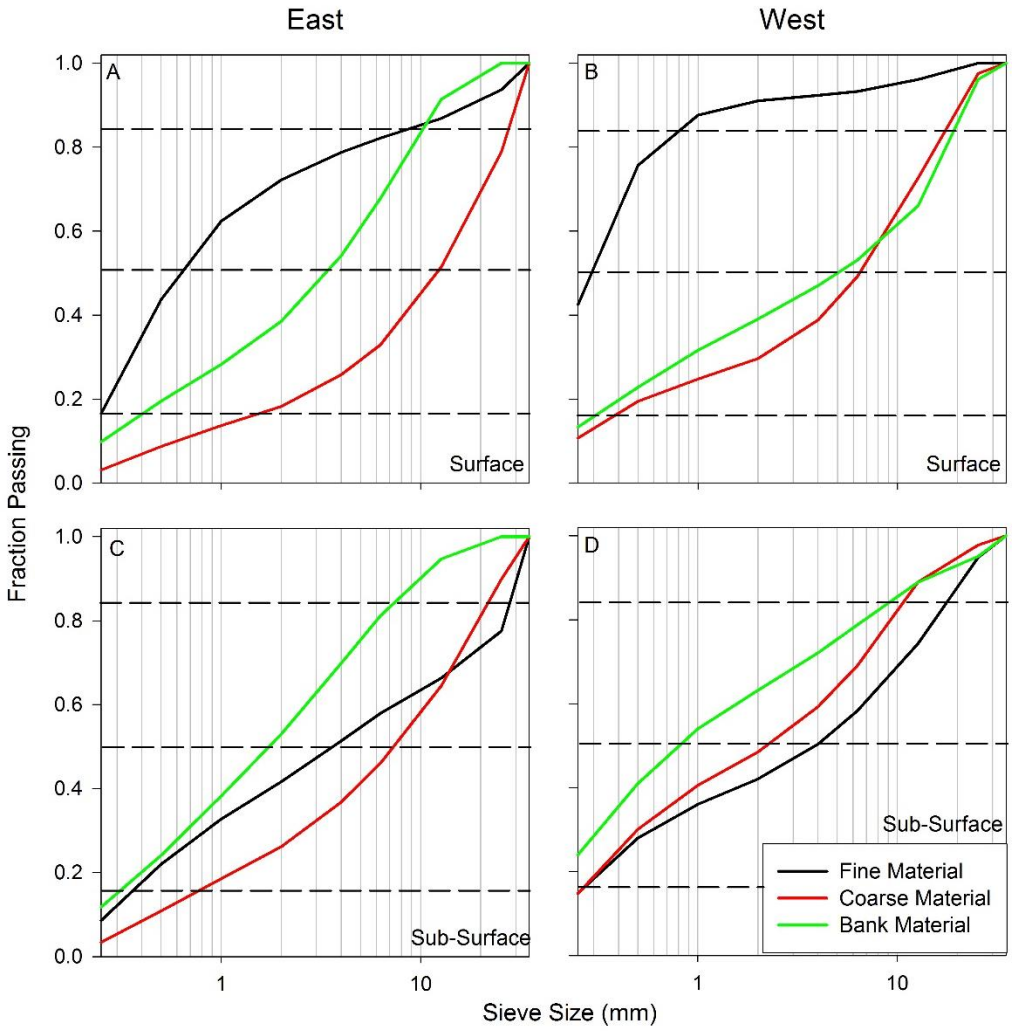

Figure 12. Sediment size distributions of sieve samples. Samples were characterized by reach, surface or sub-surface, and by sample location type. The x-axis is logarithmic to show greater detail at each end of the distribution. **A:** East surface material, **B:** West surface material, **C:** East sub-surface material, **D:** West sub-surface material.

Table 6. Sieve analysis results.

	East			West		
	D_{16} mm	D_{50} mm	D_{84} mm	D_{16} mm	D_{50} mm	D_{84} mm
Surface Fine	0.2	0.7	8.8	0.1	0.3	0.8
Surface Coarse	1.5	12.2	27.7	0.4	6.5	18.5
Surface Bank	0.4	3.5	10.7	0.3	5.1	20.3
Sub-Surface Fine	0.4	3.7	28.2	0.3	3.9	18.7
Sub-Surface Coarse	0.8	7.7	22.5	0.3	2.3	11.1
Sub-Surface Bank	0.3	1.8	7.6	0.2	0.8	9.6

The sieve analysis results were also shown in a sediment size distribution plot (Figure 12). Both branches have coarser fine material sub-surface samples than fine material surface samples. However, the opposite is true for the other two sample types. Both the coarse and the bank material have coarser distributions on the surface when compared to the sub-surface samples. These same trends are seen in Table 6 when comparing the D_{16}, D_{50}, and D_{84} of each sample type.

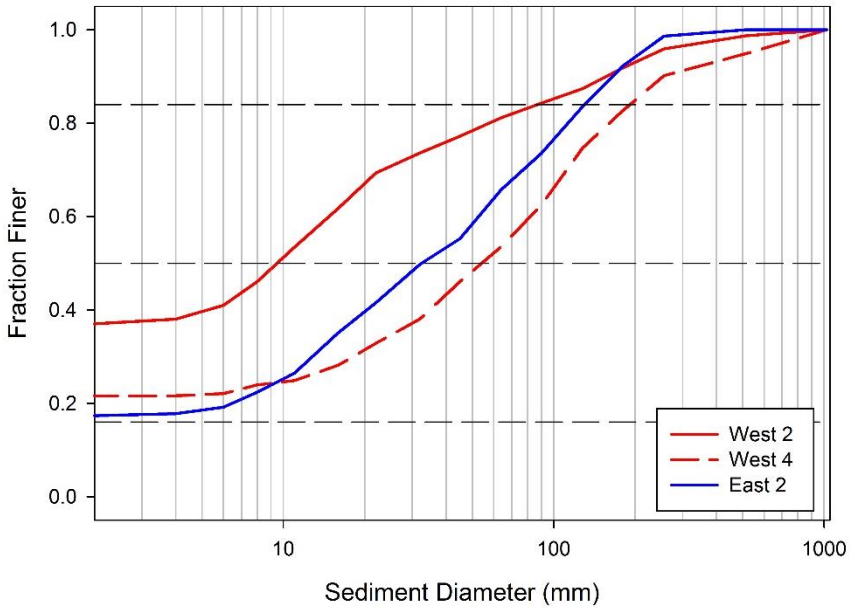

Figure 13. Pebble count sediment size distribution of the West 2, West 4, and East 2 reaches. The x-axis is plotted on a logarithmic scale to show greater detail at the ends of the distribution.

3.4. Pebble Count Results

In the pebble count results, the West 2 reach was found to be less consistently graded when compared with the other two distributions in Figure 13. The West 2 reach pebble count distribution has a large percentage of fines which skews the lower portion of the curve towards the left. The West 4 and East 2 reaches both have similar distributions. They were both uniformly graded, while the West 4 reach was found to be slightly more coarse.

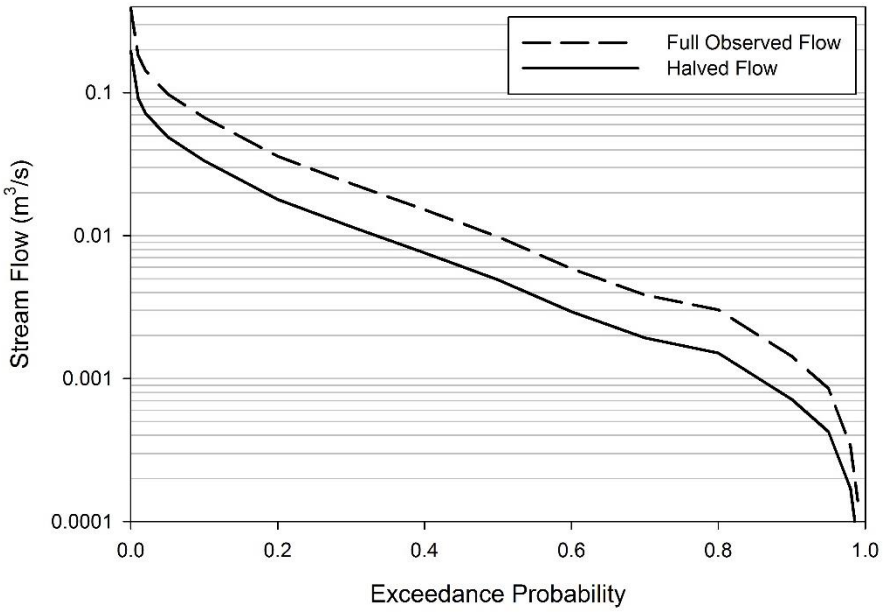

Figure 14. Flow duration curve at Crescent Stream gage. The solid line is half of the gaged flow, representing the flow that one of the branches would likely experience. The dashed line is the entire gaged flow, which represents the combination of flows from the East and West Branches.

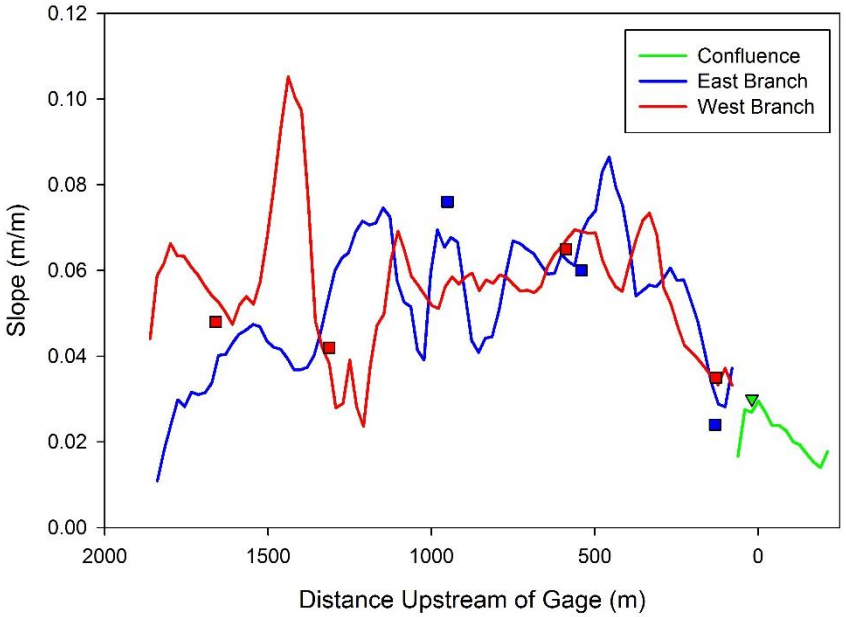

Figure 15. Slopes of confluence and each branch plotted with slopes reported in Table 5.

3.6. Sediment Mobilization Results

The slopes of the confluence reach are relatively low, which would be expected as the stream flows into Lake Fryxell. The continuous slopes shown in Figure 15 are highly variable through both the East and the West Branches. It appears that there is some correlation between the East and the West Branch slopes from 0 m to about 1000 m if the noise were averaged out. However, the deviations about the mean of the two branches appear to be uncorrelated throughout the length of each branch. As both branches approach the upstream limit, there is a significant reduction in slope. This correlates with what was observed in the field, and was the reasoning behind terminating the study reaches at these locations. The point slopes that were used in the stream power calculations appear to correlate very well with the continuous slopes plotted.

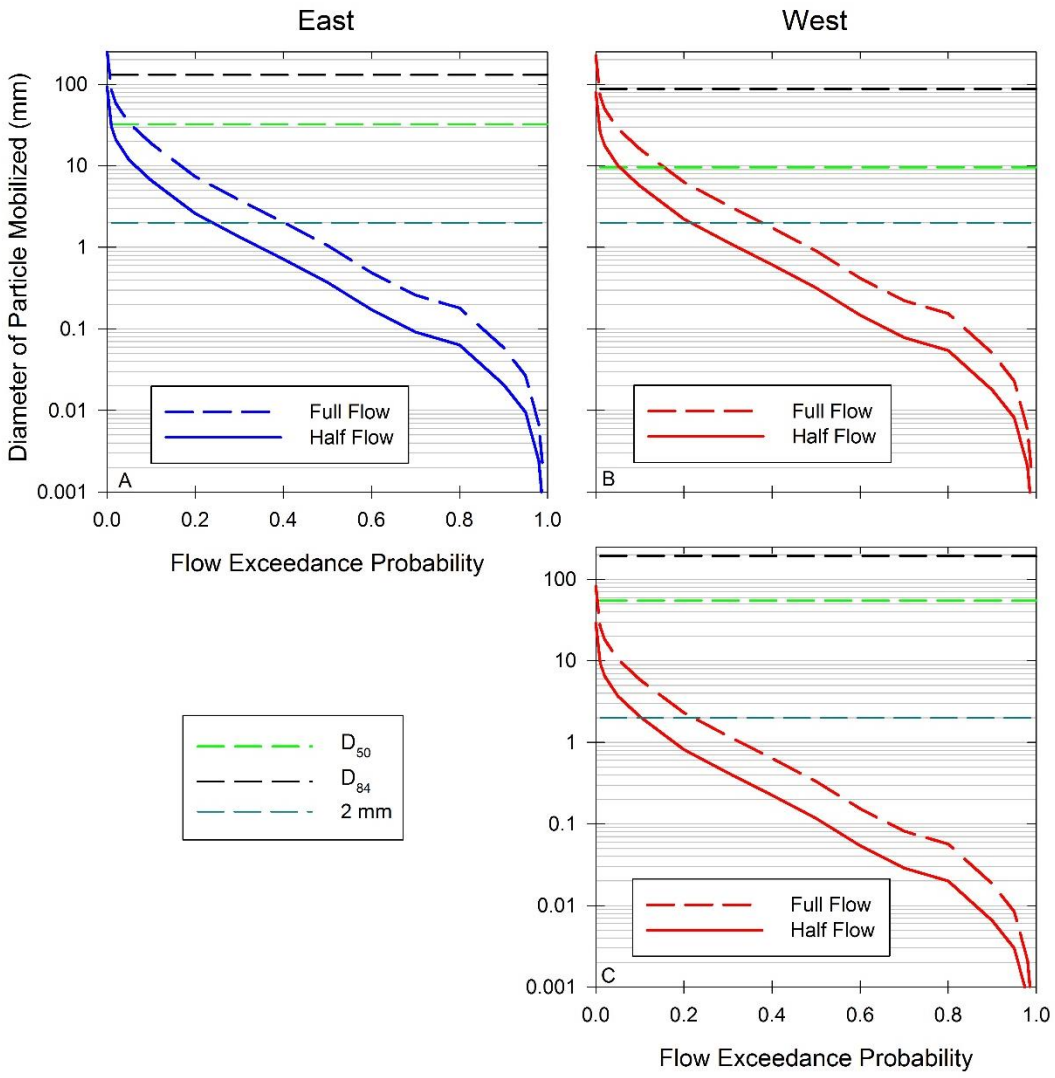

Figure 16. Particle mobilization plots. Solid curve represents half of observed flow at gage, i.e. what one branch would likely experience. Dashed curve represents a worst case scenario end member where all of the flow observed at the gage is flowing through only one of the channels. **A:** East 2 reach, **B:** West 2 reach, **C:** West 4 reach.

All of the sediment mobilization plots (Figure 16) follow the same distinct curve because of their dependence on the flow duration curve (Figure 14). The East and West 2 reaches have nearly identical curves, however the West 2 reach can more easily mobilize the finer bed material of the West Branch. The West 4 distributions are shifted significantly lower than the

other two plots due to its lower slope. Considering the maximum observed flow divided by two (the most realistic maximum flow each channel would experience) West 2 would be able to mobilize the bed material of the D_{50} particle size but not the D_{84}, West 4 would not be able to mobilize either D_{50} or D_{84} particle sizes, and East 2 would be able to mobilize the D_{50} particle size but not the D_{84} (Table 7). If all of the flow of both channels was routed through just a single channel, full gaged flow conditions, it still would take a flow with an exceedance probability of around 0.1 to mobilize the D_{50} of the East 2 reach, an exceedance probability of 0.2 to mobilize the D_{50} of the West 2 reach, and an exceedance probability of 0.01 to mobilize the D_{50} of the West 4 reach.

Table 7. Particle size mobilization.

				Max Particle Size Mobilized (mm)	
Reach	**D_{16} (mm)**	**D_{50} (mm)**	**D_{84} (mm)**	**Half Gaged Flow**	**Full Gaged Flow**
West 2	0.9	9.6	87.8	79.6	225.2
West 4	1.5	55.1	193.9	29.2	82.6
East 2	1.8	32.5	130.6	93.3	263.8

4. DISCUSSION AND CONCLUSION

4.1. Geomorphic Change Detection

Uncertainty Analysis

Geomorphic change detection was used on the LiDAR scans to investigate the volume, and rates of landform change over the past couple of years. Upon comparison of the raw results and the uncertainty analyses results in Table 4, it was clear that the uncertainty analysis of the DEMs of Difference was useful in interpretation of the results. The area of erosion in the 2012 to 2013 analyses was reduced from a raw value of 209 m^2 to around 25 m^2. This same trend was seen for the areas of erosion and deposition for both 2012 to 2013 and 2013 to 2014 analyses. This large reduction from the raw to the filtered DEM of Difference is due to the fact that the large area of false changes due to noise that were included in the raw DEM of Difference were filtered out using the uncertainty analysis. The average depth of erosion and deposition both increased from the raw DEM of Difference to the filtered DEMs of Difference. This is caused by the removal of a high number of small value changes in elevation from the raw DEM of Difference. Removing these small values increased the average distance of change. The two methods used to handle the uncertainty associated with the DEM of difference calculations yielded very similar results (Figures 6 and 7). However, it was not evident, or necessary to determine, which set of results more accurately reflects the true ground surface changes.

Rates of Geomorphic Change

The observations, and corresponding geomorphic change detection analysis made it clear that there were significant rates of ground surface change occurring on an annual timescale. The geomorphic change detection results show a significant decrease in the volume eroded from 2012 to 2013 to the volume eroded form 2013 to 2014 (Table 4). From these results, it appears the rates of topographic change due to thermokarst activity are slowing. However, the average depth of erosion remained constant at about 20 cm. This means only the area in which geomorphic change occurred decreased, while the actual linear erosion rate remained constant. Further research into the mechanisms that caused the thermokarst activity is necessary to determine why the linear retreat rates are remaining constant, while the area is decreasing.

These measured annual rates of change are comparable to measured ablation rates of ice in the form of alpine glaciers in the MDV which have been found to range from 18-40 cm/year [*Hoffman et al.*, 2008; *Bliss et al.*, 2011]. However the rates are much lower than the wasting rates of 1-3 m/year of the ice cliff in Garwood Valley [*Levy et al.*, 2013]. The erosion rates measured in this analysis and the ablation rates of ice from other studies are measuring two distinctly different scenarios. The erosion rates are believed to be caused by the thawing of ground ice or permafrost, where the ablation rates are due to the melting and sublimation of exposed ice. Although these settings are different, it is interesting that the rates of change are so similar. It may suggest a close relationship between the drivers of these processes.

Volume of Geomorphic Change

The greatest rates and volumes of geomorphic change that occurred at this location were likely undocumented because they happened shortly before the thermokarst was discovered in January of 2012. There is high uncertainty in the total ground surface changes because of the lack of pre-disturbance measurements. Since that time, the volumes and rates of the geomorphic changes have been measured. The volume of erosion decreases significantly from the 2012-2013 analysis to the 2013-2014 analysis. This result suggests that the extent of thermokarst activity in this area is actually decreasing, and the thermokarst impacted bank appears to be in the process of stabilizing.

There were relatively small volumes of deposition measured at the base of the banks where significant erosion was measured. However, the volumes of deposition measured were always much less than the volumes of erosion measured. If there was no transport of sediment in or out of the scan area, and the geomorphic change detection was perfect at calculating the volume of erosion and deposition, the volume of erosion should theoretically equal the volume of deposition, based on a theoretical mass balance. However, this is not what was observed.

There are two explanations that could cause the imbalance in between erosion and deposition. The geomorphic change detection either failed to measure the entire volume of deposition (or overestimated the volume of erosion), or some of the sediment that eroded into the channel has been transported downstream out of the area of the scans. The cause is likely a combination of these two scenarios. The depths of deposition are likely to be very small due to the dispersion of the sediment as it travels down the stream bank, and as it is transported and deposited within the channel by the stream. Therefore, true depositions measured in the raw DEM of Difference may have been discarded as unmeasurable noise in the uncertainty analysis.

However, considering that the volume of deposition measured in the raw DEM of Difference is not enough to account for all of the erosion in even the filtered DEMs of Difference, it is assumed that the majority of the sediment unaccounted for in this imbalance was transported downstream out of the area of the scans. This result suggests that the stream does have the capacity to transport the sediment out of the immediate area of the thermokarst impact. However, it does not address the extent to which the sediment inputs have been flushed through the channel.

Thermokarst Impacts on Stream Sediment

The geomorphic changes measured and observed on the West Branch of Crescent stream are evidence of significant delivery of sediment to the stream. The size of the sediment which was delivered to the stream due to thermokarst activity is assumed to have had a distribution very similar to the West Branch bank sub-surface distribution (Figure 12 D). This sediment was collected from the bank that experienced the most significant thermokarst impacts. This is the assumed distribution of the introduced sediment because the bank material, as with most other sediment throughout the MCM Dry Valleys, exhibits a desert pavement, with larger particles on the surface, and finer particles in the sub-surface. This phenomenon can be seen in the results by comparing the bank surface particle sizes to the bank sub surface particle sizes (Figure 10 E and F). The sediment eroded into the stream would be a combination of surface and sub-surface bank material, however the majority of the material would have originated from the sub-surface.

The distribution of the West Branch bank sub-surface material shows that over 60% of this material is fine (less than 2 mm). Therefore the majority of sediment introduced to the

stream due to thermokarst activity would have been fine material. This knowledge is helpful in assessing the impacts of the addition of the sediment on the stream. Knowing that the thermokarst activity introduced primarily fine sediment to the stream means that the presence of fine material on the stream bed could be considered a legacy impact of the thermokarst activity.

4.2. Sediment Size Analysis

To assess the impacts of the thermokarst activity on the West Branch of Crescent Stream, it was necessary to determine the current state of the stream bed material, as well as attempt to infer what past bed material composition may have been. The sediment size analysis of the West Branch of Crescent Stream was designed to inform the current bed material composition – as influenced by the thermokarst activity, while the investigation of the East Branch was focused on determining what the past bed material composition of the West Brach may have been. The East Branch and West Branch of Crescent Stream have many similar characteristics. They are assumed to experience equivalent amounts of flow based on field observations. The two branches have similar longitudinal profiles, and historically both have had limited sediment sources, aside from the recent thermokarst activity on the West Branch.

The fact that the sediment sources of the two branches have historically been limited may be surprising considering that these branches flow through a valley of unconsolidated sand and rock with no vegetation. However, armoring of the bed material is evident throughout each branch (Figure 11) [*McKnight et al.*, 1999]. Each branch infrequently experiences the flows necessary to mobilize this armor layer (Figure 16). Therefore, scouring of the bed or banks of the stream is not considered to be a source of readily available sediment. These branches flow

through broad channels many times the width of the actual width of the streams, and are thus disconnected from the surrounding hillslopes which limits colluvial sediment inputs. Only recently, with the thermokarst impacts on the West Branch, has there been a source of readily available sediment for the stream to transport.

Due to the similarities between the East and West Branches of Crescent Stream, and the relative stability of the East Branch, the East Branch is assumed to be an example of plausible past conditions as observed on the West Branch. There are certainly limitations to this assumption, and it cannot be fully validated. However, this relationship is a useful baseline condition to compare the impacted West Branch to. The location of the furthest upstream reach of the West Branch was chosen to be located just downstream of a flat depositional zone (Figures 9 B and 15). This is important because it is assumed that the flat depositional zone settles out the majority of the sediment that may have been introduced upstream, thus allowing each upstream reach to be considered an upstream boundary condition of zero sediment flux. This allows the West 4 reach to be used as another example of background conditions on the West Branch with minimal impacts due to thermokarst activity. In reality there is likely a small amount of sediment transport from upstream past this depositional zone into reach West 4, however there was minimal documented thermokarst activity upstream of this reach in January 2012, which further validates this assumption.

Reach Averaged Percent Fines Distributions

The average percent fines composition of the West 4 reach was very similar to the percent fines of all East reaches. This result is important because it helps to validate the assumption that the West 4 reach can be considered an example of a West Branch reach that has not been impacted by thermokarst activity. West 4 had the coarsest pebble count measured out of the three reaches that were sampled using this method. This result is caused by the lack of sediment sources available to this reach. As demonstrated in Figure 16, this reach can rarely mobilize the bed material, and it likely receives very little sediment from upstream. The West 3 reach exhibits a spike in the average percent fine value, accompanied with a large standard deviation of the percent fine values. This result is likely due to an upstream source of fine sediment due to thermokarst activity, as well as the relatively low slope of this reach. The lower slope results in a lower capacity of the stream to transport sediment, which may result in a higher percentage of fine values.

The West 2 reach exhibits a significant reduction in the average percent fine value from the West 3 reach. This result is likely due to the fact that West 2 has a higher slope than West 3. However, the West 2 reach has a higher average percent fines value than all of the east branch reaches. This higher average percent fines value is due to upstream introduction of fine sediment from thermokarst activity. West 1 has a relatively low slope, but it has an average percent fine value that is still greater than all of the east branch reaches, even East 1 which has a lower slope. The confluence also exhibits an average percent fine value larger than the entire East Branch. It may be argued that the confluence has a low slope and would be expected to have a high value of average percent fine, however the East 1 Branch has a lower slope and still a lower percentage of fines.

The East Branch is assumed to be a surrogate for the past conditions on the West Branch. All reaches on the east branch exhibited a constant reach averaged percent fine value and similarly small standard deviations. This was a surprising result based on the wide range of slopes sampled on the East Branch. This result suggests that the bed material composition of this branch is relatively static and stable throughout the length of the branch, and the slope of the channel has a minimal effect on the percentage of fines on the bed for this branch. The stability of this branch is likely due to the bed armoring and the inability of the channel to mobilize the coarse armor material.

From the pebble counts and the fine sediment counts, it is clear that the West Branch contains much more fine material than the east branch. Regardless of the varying slopes and upstream conditions this trend holds true. The main difference between these two branches that has the potential to cause this difference in the amount of fine sediment in each branch is the presence of thermokarst activity on the West Branch. It is apparent that the increased amount of fine sediment on the West Branch is a direct result of the thermokarst activity.

Sediment Mobilization Capacity

The sediment mobilization analysis was designed to assess the extent to which the stream has the ability to transport its own bed material, and the sediment introduced by the thermokarst activity. Stream power was used because it allows for the estimation of particle size mobilization using gross channel parameters that were relatively simple to measure. Calculation of stream power (Eq. 1) requires three parameters: slope (S), discharge (Q), and width (w). The simplicity of these parameters is useful in this situation because other bed-load transport equations utilize shear stress which requires knowledge of the depth and wetted perimeter, which

are much more difficult to estimate, especially with the shallow, low flows experienced on Crescent Stream.

The results of this analysis are shown in Figure 16 and Table 7. The equations used to calculate the bed material size mobilized by a given flow required knowledge of the particle size responsible for grain roughness, in the Manning-Strickler grain roughness relation. This required the bed material size distribution of the reach, therefore only the reaches where true pebble counts were taken could be analyzed (East 2, West 2, and West 4). The flows used to inform the stream power calculations were taken from the flow duration curve (Figure 14). The solid line represents the realistic flows that each channel might experience, which is half of the gaged (total) flow. The dotted line represents a maximum end member, in the unlikely event in which all of the flow seen at the gage is flowing through one channel.

The calculated bed material particle size mobilization of the East 2 and West 2 reaches were very similar (Figure 16). This is because they have very similar slopes, discharges, and widths. However, the East 2 reach is able to mobilize its bed material much less frequently because of how much larger its bed material size distribution is than the West 2 reach. The West 4 reach has a curve that is shifted lower than the other two reaches due to its lower slope. This is interesting because the West 4 reach has the largest bed material sizes. Under the likely flow conditions, where half of the gaged flow is coming from the West Brach, the West 4 reach would be unable to mobilize its D_{50} particle size even if it were experiencing the largest flow ever observed on Crescent Stream.

According to sediment size mobilization plots, the mobilization of the D_{50} bed material size is relatively infrequent. This is a good illustration of why the channels experience armoring, and how they remain static over long periods of time. The equation used to calculate the particle

sizes that could potentially be mobilized has inherent limitations and was designed for gravel sized particles, not sand size or smaller particles on the order of 2 mm. However, the 2 mm line was included as a reference to show how infrequently even fine particles would be mobilized in these reaches. These plots suggest that if the thermokarst activity did introduce large amounts of sediment to the stream, the stream does have the potential to transport this material downstream. However, the probability of exceeding the flows necessary to transport this material is relatively low, suggesting that most of what the thermokarst activity introduced would still be in the channel after only a couple of seasons of flow. This conclusion is further supported by the increased amount of fine material found throughout the West Branch.

Comparison of GCD and Sediment Size Analysis

The results of the GCD and the sediment size analysis appear to be contradictory. The GCD analysis shows very little aggradation in the scan area, while the increased amount of fine sediment found in the West Branch could be interpreted as aggradation of fine material on the bed surface. However, it should be noted that if aggradation of fine sediment did occur within the stream channel, the GCD analysis would have trouble detecting small changes. One drawback of the TLS technology is that it cannot penetrate water. Therefore, the point density is very low wherever water was present within the channel at the time of the scan. The magnitude of the aggradation also makes it difficult to detect with the GCD analysis. The aggradation of the bed is likely a small change on the order of a couple of centimeters distributed over a large area. These small changes are discarded with the minLoD analysis which discards any changes detected less than 10 cm. The FIS analysis does a slightly better job in accepting smaller changes, however it is still limited by low point density within the channel. The GCD analysis

more accurately illustrates the changes that have occurred outside of the channel, whereas the sediment size analysis explains the changes that have occurred within the channel.

Ecosystem Implications

The biological communities of Crescent Stream and Lake Fryxell continue to be impacted by the thermokarst activity on Crescent Stream, because of the continued impacts still observed throughout the stream. The immediate massive amount of sediment introduced, sometime shortly before January of 2012, undoubtedly had serious impacts on the stream biota. This event likely buried and scoured algae on the bed material, while limiting the amount of sunlight due to higher turbidity. However, this analysis has shown the stream is still in the process of flushing the sediment through the channel, which continues to have a negative impact on the stream biota. As shown in Figure 16 the increased fine sediment of West 2 causes the bed material to be mobilized much more frequently than the bed material of East 2 and West 4. This presents a problem for algae trying to populate the substrate [*Alger et al.*, 1997]. With more mobile bed material there remains the potential for the burial or scouring of algae. Further research is needed to quantify the ecologic impacts of the thermokarst disturbances, because based on field observations there was a distinct lack of algae on the West Branch compared to the East Branch. With a warming climate the initiation of thermokarst features is only expected to increase in this region, which will challenge the resiliency of more MDV streams and their dependent biologic communities.

4.3. Conclusion

The West Branch of Crescent Stream is still experiencing geomorphic changes on the banks due to thermokarst activity since the initial discovery of massive bank failures in January of 2012. The linear rates of erosion and deposition of 20 cm and 10 cm respectively, appear to be holding constant from year to year, however the areal extent impacted by surface change has decreased from an average of 24.5 m^2 to 10.3 m^2 from 2012-2013 to 2013-2014 respectively. The impacts of the thermokarst activity are still observed throughout the West Branch of Crescent Stream in the form of fine material on the stream bed. The limited flows of Crescent Stream have been able to transport some of this newly introduced fine material downstream, however the bed material size of the West Branch still remains finer than the East Branch due to the sediment introduced by the thermokarst activity. Crescent Stream continues to adjust to the impacts of the thermokarst activity influencing the biota the stream supports. With a warming climate, this scenario is expected to become more common throughout the MDV.

REFERENCES

Alger, A. S., D. M. McKnight, S. A. Spalding, C. M. Tate, G. H. Shupe, K. A. Welch, R. Edwards, E. D. Andrews, and H. R. House (1997), *Alger et al.pdf*, Boulder, CO.

Bagnold, R. A. (1980), An Empirical Correlation of Bedload Transport Rates in Flumes and Natural Rivers, *Proc. R. Soc. London A Math. Phys. Eng. Sci.*, *372*(1751), 453–473.

Barnhart, T., and B. Crosby (2013), Comparing Two Methods of Surface Change Detection on an Evolving Thermokarst Using High-Temporal-Frequency Terrestrial Laser Scanning, Selawik River, Alaska, *Remote Sens.*, *5*(6), 2813–2837, doi:10.3390/rs5062813.

Bater, C. W., and N. C. Coops (2009), Evaluating error associated with lidar-derived DEM interpolation, *Comput. Geosci.*, *35*, 289–300, doi:10.1016/j.cageo.2008.09.001.

Bliss, A. K., K. M. Cuffey, and J. L. Kavanaugh (2011), Sublimation and surface energy budget of Taylor Glacier, Antarctica, *J. Glaciol.*, *57*(204), 684–696, doi:10.3189/002214311797409767.

Bowden, W. B., M. N. Gooseff, a. Balser, a. Green, B. J. Peterson, and J. Bradford (2008), Sediment and nutrient delivery from thermokarst features in the foothills of the North Slope, Alaska: Potential impacts on headwater stream ecosystems, *J. Geophys. Res. Biogeosciences*, *113*, 1–12, doi:10.1029/2007JG000470.

Bunte, K., and S. R. Abt (2001), *Sampling Surface and Subsurface Particle-Size Distributions in Wadable Gravel- and Cobble-Bed Streams for Analyses in Sediment Transport , Hydraulics , and Streambed Monitoring*, Fort Collins, CO.

Conovitz, P. A., D. M. Mcknight, L. H. Macdonald, and A. G. Fountain (1998), Hydrologic Processes Influencing Streamflow Variation in Fryxell Basin, Antarctica, in *Ecosystem Dynamics in a Polar Desert: The McMurdo Dry Valleys, Antarctica*, pp. 93–108.

ESRI (2012), ArcMap 10.1.

Ferguson, R. I. (2005), Estimating critical stream power for bedload transport calculations in gravel-bed rivers, *Geomorphology*, *70*, 33–41, doi:10.1016/j.geomorph.2005.03.009.

Foreman, C. M., C. F. Wolf, and J. C. Priscu (2004), Impact of episodic warming events on the physical , chemical and biological relationships of lakes in the McMurdo Dry Valleys, Antarctica, *Aquat. Geochemistry*, *10*, 239–268, doi:10.1007/s10498-004-2261-3.

Fountain, A. G. et al. (1999), Physical Controls on the Taylor Valley Ecosystem, Antarctica, *Bioscience*, *49*(12), 961, doi:10.2307/1313730.

Fountain, A. G., J. S. Levy, M. N. Gooseff, and D. Van Horn (2014), The McMurdo Dry Valleys: A landscape on the threshold of change, *Geomorphology*, *225*, 25–35, doi:10.1016/j.geomorph.2014.03.044.

Gooseff, M. N., D. M. McKnight, P. Doran, A. G. Fountain, and W. B. Lyons (2011), Hydrological connectivity of the landscape of the McMurdo Dry Valleys, Antarctica, *Geogr. Compass*, *5*, 666–681, doi:10.1111/j.1749-8198.2011.00445.x.

Hoffman, M. J., A. G. Fountain, and G. E. Liston (2008), Surface energy balance and melt thresholds over 11 years at Taylor Glacier, Antarctica, *J. Geophys. Res. Earth Surf.*, *113*(4), 1–12, doi:10.1029/2008JF001029.

Julien, P. (2010), *Erosion and Sedimentation*, Second Edi., Cambridge University Press.

Kokelj, S. V., and M. T. Jorgenson (2013), Advances in thermokarst research, *Permafr. Periglac. Process.*, *24*(2), 108–119, doi:10.1002/ppp.1779.

Kokelj, S. V., T. C. Lantz, J. Kanigan, S. L. Smith, and R. Coutts (2009), Origin and polycyclic behaviour of tundra thaw slumps, Mackenzie Delta region, Northwest Territories, Canada, *Permafr. Periglac. Process.*, *20*(2), 173–184, doi:10.1002/ppp.642.

Kokelj, S. V., D. Lacelle, T. C. Lantz, J. Tunnicliffe, L. Malone, I. D. Clark, and K. S. Chin (2013), Thawing of massive ground ice in mega slumps drives increases in stream sediment and solute flux across a range of watershed scales, *J. Geophys. Res. Earth Surf.*, *118*(2), 681–692, doi:10.1002/jgrf.20063.

Levy, J. S., a G. Fountain, J. L. Dickson, J. W. Head, M. Okal, D. R. Marchant, and J. Watters (2013), Accelerated thermokarst formation in the McMurdo Dry Valleys, Antarctica., *Sci. Rep.*, *3*, 2269, doi:10.1038/srep02269.

Marchant, D. R., and J. W. Head (2007), Antarctic dry valleys: Microclimate zonation, variable geomorphic processes, and implications for assessing climate change on Mars, *Icarus*, *192*, 187–222, doi:10.1016/j.icarus.2007.06.018.

McKnight, D. M. (2014), Crescent Stream Gage Measurements: McMurdo Dry Valleys LTER, *NSF*.

McKnight, D. M., D. K. Niyogi, A. S. Alger, A. Bomblies, P. a. Conovitz, and C. M. Tate (1999), Dry Valley Streams in Antarctica: Ecosystems Waiting for Water, *Bioscience*, *49*(12), 985, doi:10.2307/1313732.

Schenk, T., B. M. Csatho, Y. Ahn, T. Yoon, and W. S. Shin (2004), DEM generation from the Antarctic LiDAR data: Site report, *USGS*.

Wheaton, J. M. (2015), Geomorphic Change Detection Software, *Utah State University*.

Wheaton, J. M., J. Brasington, S. E. Darby, and D. a. Sear (2009), Accounting for uncertainty in DEMs from repeat topographic surveys: improved sediment budgets, *Earth Surf. Process. Landforms*, *156*(December 2009), n/a–n/a, doi:10.1002/esp.1886.